

# High-order accurate entropy stable schemes for compressible Euler equations with van der Waals equation of state on adaptive moving meshes

Shangting Li

*Center for Applied Physics and Technology, HEDPS and LMAM, School of Mathematical Sciences, Peking University, Beijing 100871, P.R. China*

Huazhong Tang\*

*Nanchang Hangkong University, Jiangxi Province, Nanchang 330000, P.R. China; Center for Applied Physics and Technology, HEDPS and LMAM, School of Mathematical Sciences, Peking University, Beijing 100871, P.R. China*

---

## Abstract

This paper develops the high-order entropy stable (ES) finite difference schemes for multi-dimensional compressible Euler equations with the van der Waals equation of state (EOS) on adaptive moving meshes. Semi-discrete schemes are first nontrivially constructed built on the newly derived high-order entropy conservative (EC) fluxes in curvilinear coordinates and scaled eigenvector matrices as well as the multi-resolution WENO reconstruction, and then the fully-discrete schemes are given by using the high-order explicit strong-stability-preserving Runge-Kutta time discretizations. The high-order EC fluxes in curvilinear coordinates are derived by using the discrete geometric conservation laws and the linear combination of the two-point symmetric EC fluxes, while the two-point EC fluxes are delicately selected by using their sufficient condition, the thermodynamic entropy and the technically selected parameter vector. The adaptive moving meshes are iteratively generated by solving the mesh redistribution equations, in which the fundamental derivative related to the occurrence of non-classical waves is involved to produce high-quality mesh. Several numerical tests on the parallel computer system with the MPI programming are conducted to validate the accuracy, the ability to capture the classical and non-classical waves, and the high efficiency of our schemes in comparison with their counterparts on the uniform mesh.

*Keywords:* Entropy stable scheme, entropy conservative scheme, mesh redistribution, van der Waals equation of state

---

\*Corresponding author. Fax: +86-10-62751801.

*Email addresses:* [shangtl@pku.edu.cn](mailto:shangtl@pku.edu.cn) (Shangting Li), [hztang@math.pku.edu.cn](mailto:hztang@math.pku.edu.cn) (Huazhong Tang)

## 1. Introduction

This paper is concerned with high-order accurate entropy stable (ES) schemes to the compressible Euler equations with the van der Waals equation of state (EOS), which are given by

$$\frac{\partial \mathbf{U}}{\partial t} + \sum_{k=1}^d \frac{\partial \mathbf{F}_k(\mathbf{U})}{\partial x_k} = 0, \quad d = 1, 2, 3, \quad (1.1)$$

$$\mathbf{U} = (\rho, \rho \mathbf{v}^T, E)^T, \quad (1.2)$$

$$\mathbf{F}_k = (\rho v_k, \rho v_k \mathbf{v}^T + p \mathbf{e}_k^T, (E + p)v_k)^T, \quad (1.3)$$

and

$$p = \frac{\rho R T}{1 - \rho b} - a \rho^2, \quad e = c_v T - a \rho, \quad (1.4)$$

where  $\rho$ ,  $\mathbf{v} = (v_1, \dots, v_d)^T$ ,  $T$ , and  $E = \rho e + \rho |\mathbf{v}|^2/2$  are the density, the velocity vector, the temperature, and the total energy, respectively. Moreover,  $\mathbf{e}_k$  denotes the  $k$ th column of the  $d \times d$  unit matrix,  $e$  is the specific internal energy,  $R$  is the positive gas constant,  $c_v$  is the specific heat at constant volume, and  $a \geq 0$  and  $b \geq 0$  are two van der Waals constants depending on the intermolecular forces and the size of the molecules. Obviously, when  $a = 0$  and  $b = 0$ , the van der Waals EOS (1.4) reduces to the ideal gas law. The van der Waals EOS is often used to depict the potentially non-classical phenomena (occurrences of non-classical waves) above the saturated vapour curve near the thermodynamic critical point and has important applications in engineering such as heavy gas wind tunnels and organic Rankine cycle engines [2, 56, 18]. Several researchers investigated the creation and evolution of the non-classical waves [4, 36, 61, 19, 20, 46], and studied the numerical schemes such as the TVDM (total variation diminishing MacCormack) methods [3, 9, 10] and the Roe type schemes [1, 27, 29, 17, 30] for the compressible Euler equations with the van der Waals EOS.

The van der Waals EOS (1.4) can be rewritten into a cubic equation with respect to the specific volume  $\nu := 1/\rho$  as follows

$$\nu^3 - \left(b + \frac{RT}{p}\right) \nu^2 + \frac{a}{p} \nu - \frac{ab}{p} = 0, \quad (1.5)$$

so that the roots for the specified gas at a given pressure are no more than three cases: three identical real roots, three different real roots, and one real root and two imaginary roots [44]. The thermodynamic critical point at the critical temperature  $T_c$  (where the derivatives  $p_\nu$  and  $p_{\nu\nu}$  are zero) corresponds to the case of that the cubic equation (1.5) has three identical real roots, and thus the van der Waals constants  $a$  and  $b$  can be obtained by analyzing (1.5) at such critical point

as follows

$$b = \frac{1}{3\rho_c}, \quad a = \frac{9p_c}{8Z_c\rho_c^2}, \quad Z_c = \frac{p_c}{R\rho_c T_c} = \frac{3}{8}, \quad (1.6)$$

where  $p_c$  and  $\rho_c$  are the critical pressure and density, respectively, and will be used to non-dimensionalize the compressible Euler equations with the van der Waals EOS (1.1)-(1.4) in the next section.

This paper only considers the van der Waals gas, whose physically admissible state should satisfy

$$0 < \rho < 1/b, \quad T > T_0, \quad RT - 2a\rho(1 - b\rho)^2 > 0. \quad (1.7)$$

In fact, the van der Waals EOS (1.4) implies that the pressure  $p$  is positive at any volume if  $0 < \rho < 1/b$  and  $RT - a\rho(1 - b\rho) > 0$ . The term  $RT - a\rho(1 - b\rho)$  can be viewed as the quadratic equation about  $\rho$  so that the expression  $RT - a\rho(1 - b\rho)$  is always positive if its discriminant  $-4abRT + a^2 < 0$ , i.e.

$$T > T_0 := \frac{a}{4Rb}. \quad (1.8)$$

So, one has  $p > 0$  if  $0 < \rho < 1/b$  and  $T > T_0$ . On the other hand, from the fact that the product of the thermal expansion coefficient  $-\frac{1}{\rho}(\partial_T \rho)|_p$  and the Grüneisen coefficient  $\frac{1}{\rho}(\partial_e p)|_\rho$  is nonnegative [47], i.e.

$$\left(-\frac{1}{\rho}(\partial_T \rho)|_p\right) \left(\frac{1}{\rho}(\partial_e p)|_\rho\right) = \left(\frac{R(1 - b\rho)}{RT - 2a\rho(1 - b\rho)^2}\right) \left(\frac{\delta}{1 - b\rho}\right) \geq 0,$$

with  $\delta = \gamma - 1 = R/c_v > 0$ , one has

$$RT - 2a\rho(1 - b\rho)^2 > 0,$$

here the case of  $RT - 2a\rho(1 - b\rho)^2 = 0$  has been excluded, relating to the infinite thermal expansion coefficient happening at the critical points.

Additionally, it is worth noting that the fundamental derivative  $G$  introduced by [54] is a vital parameter governing the nonlinear dynamics of gases

$$G = \frac{\nu^3}{2c_s^2} \left(\frac{\partial^2 p}{\partial \nu^2}\right)_s = 1 + \frac{\rho}{c_s} \left(\frac{\partial c_s}{\partial \rho}\right)_s, \quad (1.9)$$

where  $c_s$  and  $s$  are respectively the speed of sound and the specific entropy and expressed as

$$c_s = \left[(\delta + 1) \frac{RT}{(1 - b\rho)^2} - 2a\rho\right]^{1/2}, \quad s = c_v \ln T - R \ln(\nu - b).$$

The sign of  $G$  can be viewed as a parameter related to the occurrence of non-classical waves such as the expansion shocks etc. To show that, by using the Taylor expansion and the Rankine-Hugoniot jump conditions for a weak shock wave, the relationship between the entropy change  $\Delta s$  and the specific volume change  $\Delta \nu$  is given as follows [4]

$$\Delta s = - \left( \frac{\partial^2 p}{\partial \nu^2} \right)_s \frac{(\Delta \nu)^3}{12T_f} + \mathcal{O}(\Delta \nu^4),$$

where  $\left( \frac{\partial^2 p}{\partial \nu^2} \right)_s$  presents the isentropic curvature which may be 0 at the critical point and  $T_f$  is the temperature before the shock wave. Neglecting the term  $\mathcal{O}(\Delta \nu^4)$ , one may have the following result. For the ideal gas away from the critical point, it has  $\left( \frac{\partial^2 p}{\partial \nu^2} \right)_s > 0$ , equivalently  $G > 0$ . Thus, if  $\Delta \nu < 0$ , then  $\Delta s > 0$  and a compressive shock wave is formed. For the gas with sufficiently large specific heats, the isentropic curvature  $\left( \frac{\partial^2 p}{\partial \nu^2} \right)_s$  and  $G$  may be negative, so  $\Delta s$  may be positive and the expansion shock wave without violating the entropy conditions may be formed when  $\Delta \nu > 0$ .

For the hyperbolic system (1.1)-(1.4), the physically relevant solutions may be discontinuous even if the initial data are smooth, so one should consider weak solutions which are not unique in general, and the entropy conditions satisfied by non-classical and classical waves are the significant property to single out the physically relevant solution out of weak solutions.

To select the physically relevant solution out of all weak solutions, it is significant to construct the ES schemes satisfying discrete or semi-discrete entropy conditions. For the scalar conservation laws, the fully-discrete monotone conservative schemes can converge to the entropy solution satisfying the entropy conditions [21, 31]. Semi-discrete E-schemes [42, 43] satisfy the entropy conditions for any convex entropy pairs. For the system of hyperbolic conservation laws, the semi-discrete second-order entropy conservative (EC) scheme satisfying the entropy identity was constructed in [49, 50], and the higher-order extension was proposed in [37]. In order to suppress possible oscillations near the discontinuities, with the help of the “sign” property of the ENO reconstruction, some numerical dissipative terms were added to EC schemes to get the semi-discrete ES schemes [25]. The ES schemes were also extended to the ES discontinuous Galerkin (DG) based on the summation-by-parts operators [34, 26, 13, 16]. Recently, the EC or ES schemes were constructed for the (multi-component) compressible Euler equations [35, 15, 40], the relativistic (magneto)hydrodynamic equations [5, 60, 22, 23], and so on. In a mimicking manner, the energy stable schemes for the shallow water equations could also be developed, see [24, 63, 64].

In order to improve the efficiency and quality of the numerical solutions, adaptive moving mesh methods are considered, which play an important role in solving partial differential equations, including the grid redistribution approaches [7, 8, 45, 57, 59], the moving mesh PDEs methods [12, 14, 48], and [22, 39, 32, 33, 38, 51, 52]. For more details, readers are referred to the review

articles [11, 53] for more exhaustive treatments.

This paper focuses on constructing high-order adaptive moving mesh ES schemes for the compressible Euler equations with the van der Waals EOS. Technically constructing the two-points EC fluxes is the key point which is difficult due to the non-linearity arising from the van der Waals EOS (1.6). The explicit form of the two-points symmetric EC fluxes in non-dimensional variables is first derived based on the carefully chosen parameter vectors and the thermodynamic entropy under rational conditions. Utilizing the linear combination of the two-points fluxes and the high-order discrete geometric conservation laws, the high-order EC fluxes in curvilinear coordinates are constructed. To avoid numerical oscillations near non-classical and classical waves, the high-order dissipation terms, based on the newly derived complex scaled eigenmatrix and the multi-resolution WENO reconstruction [58], are added to the high-order EC fluxes to obtain the semi-discrete high-order ES schemes satisfying the entropy inequality. The mesh adaptation is implemented by iteratively solving the Euler-Lagrange equations of the mesh adaptation functional with appropriate monitor function, clustering the mesh in the region of interest. The monitor function is related to the fundamental derivative  $G$  given in (1.9), so the mesh can concentrate around the region where  $G$  changes to capture the non-classical wave appearing in the van der Waals gas, which improves the performance of the solution. The explicit third-order strong-stability-preserving Runge-Kutta (SSP-RK) method [28] is used for the time discretization. Several numerical results are provided to verify the efficiency of our schemes, which outperform their counterparts on a uniform mesh implemented on a parallel computer using MPI programming.

This paper is organized as follows. Section 2 gives the dimensionless versions of the governing equations (1.1)-(1.4) in Cartesian and curvilinear coordinates, corresponding entropy conditions, and the physically admissible state. Section 3 derives the explicit expression of the two-points symmetric EC flux by solving a linear algebraic system deduced by the chosen parameter vector, and then constructs the high-order EC and ES schemes for the compressible Euler equations with the van der Waals EOS in curvilinear coordinates. Section 4 presents the adaptive moving mesh strategy. Several numerical results are presented in Section 5 to validate the performance of high-order adaptive moving mesh ES schemes. Some conclusions are given in Section 6.

## 2. Entropy conditions

This section introduces the dimensionless forms of the system (1.1)-(1.4) in Cartesian and curvilinear coordinates, and corresponding entropy conditions. If the following non-dimensional thermodynamic variables

$$p_* = \frac{p}{p_c}, \quad \rho_* = \frac{\rho}{\rho_c}, \quad T_* = \frac{T}{T_c}, \quad v_{k,*} = \frac{v_k}{(RT_c)^{1/2}},$$

$$e_* = \frac{e}{RT_c}, \quad s_* = \frac{s - s_c}{R}, \quad c_{s,*} = \frac{c_s}{(RT_c)^{1/2}},$$

are used, then the conservative variable vector  $\mathbf{U}$  and the flux vectors  $\mathbf{F}_k$  in (1.1)-(1.3) can be rewritten in dimensionless form [9] as follows

$$\begin{aligned} \mathbf{U}_* &= [\rho_*, \rho_* \mathbf{v}_*^T, E_*]^T, \\ \mathbf{F}_{k,*} &= \left[ \rho_* v_{k,*}, \rho_* v_{k,*} \mathbf{v}_*^T + \frac{3}{8} p_* \mathbf{e}_k^T, \left( E_* + \frac{3}{8} p_* \right) v_{k,*} \right]^T. \end{aligned} \quad (2.1)$$

Utilizing the van der Waals constants  $a, b$  given in (1.6), the van der Waals EOS (1.4) can be reformulated as

$$p_* = \frac{1}{p_c} \left( \frac{R \rho_c T_c \rho_* T_*}{1 - 1/3 \rho_*} - \frac{3 p_c}{\rho_c^2} \rho_*^2 \rho_*^2 \right) = \frac{8 \rho_* T_*}{3 - \rho_*} - 3 \rho_*^2, \quad (2.2)$$

$$e_* = \frac{c_v T_c T_*}{RT_{cr}} - \frac{3 p_c}{\rho_c} \frac{1}{RT_c} \rho_* = \frac{T_*}{\delta} - \frac{9}{8} \rho_*, \quad (2.3)$$

and the fundamental derivative, the thermodynamic entropy and the speed of sound in the non-dimensional variable form can be given by

$$\begin{aligned} G_* &= \frac{(\delta + 1)(\delta + 2) \frac{p_c p_* + 3 p_c \rho_*^2}{(1/\rho_* - 1/3)^2 1/\rho_c^2} - 18 p_c \rho_c^2 \rho_*^4}{2(\delta + 1) \rho_c^2 \frac{p_c p_* + 3 p_c \rho_*^2}{1/\rho_* (1/\rho_* - 1/3)} - 12 p_c \rho_c^2 \rho_*^4} \\ &= \frac{27}{2(c_{s,*})^2} \left[ \left( \frac{1}{3 - \rho_*} \right)^3 (2 + 3\delta + \delta^2) T_* - \frac{\rho_*}{4} \right], \\ s_* &= \frac{\ln T_*}{\delta} + \ln \left( \frac{3 - \rho_*}{2 \rho_*} \right), \\ c_{s,*} &= \frac{1}{(RT_c)^{1/2}} \left[ \frac{(\delta + 1) RT_*}{\left(1 - \frac{1}{3} \rho_*\right)^2} - 2 \frac{3 p_c}{\rho_c} \rho_* \right]^{1/2} = \left[ (\delta + 1) T_* \left( \frac{3}{3 - \rho_*} \right)^2 - \frac{9}{4} \rho_* \right]^{1/2}. \end{aligned}$$

One can derive that the entropy  $s_*$  satisfies

$$\partial_{t_*} s_* + \sum_{k=1}^d v_{k,*} \frac{\partial s_*}{\partial x_{k,*}} \geq 0,$$

or

$$\frac{\partial(\rho_* s_*)}{\partial t_*} + \sum_{k=1}^d \frac{\partial(\rho_* s_* v_{k,*})}{\partial x_{k,*}} \geq 0.$$

In the subsequent discussion, the subscript  $*$  will be omitted for convenience, unless otherwise stated.

**Remark 2.1.** The inequalities (1.7) and (1.8) in the dimensionless variable form become

$$T > T_0 = 27/32, \quad 4T - \rho(3 - \rho)^2 > 0,$$

respectively, so the dimensionless solution for the van der Waals gas should satisfy them and  $3 > \rho > 0$ .  $\square$

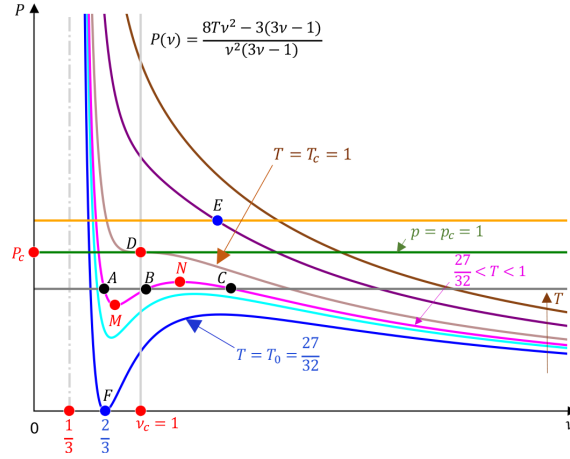


Figure 2.1: The curves of the pressure  $p = 8T/(3\nu - 1) - 3/\nu^2$  with respect to specific volume  $\nu = 1/\rho$  at different temperature  $T$ .

**Remark 2.2.** The admissible states for the van der Waals gas can be further discussed by observing the  $p$ - $\nu$  curves in Figure 2.1, similar to those in [44, Fig.1]. For the van der Waals gas, see Remark 2.1, the slope of the  $p$ - $\nu$  curve

$$p_\nu = -6 \times \frac{4T\nu^3 - (3\nu - 1)^2}{(3\nu - 1)^2}, \quad (2.4)$$

should be less than zero. The point D is the thermodynamic critical point at the critical temperature  $T_c$ , where both the first- and second-order derivatives  $p_\nu$  and  $p_{\nu\nu}$  are 0, so the temperature  $T_D = T_c = 1$ . The left and right sides of the point D correspond to the liquid and gas, respectively. The  $p$ - $\nu$  curves at the upper right side of the isotherm  $T_c$  are the isotherms with  $T > T_c = 1$ , corresponding to the gas and satisfying  $p_\nu < 0$  when  $\nu > 1/3$ . The isotherm with  $T \geq T_c$  has only one intersection point such as the point E with the isobaric line (the horizontal line), that is, the value of  $\nu$  is uniquely determined if  $p$  and  $T$  are given. The point F is the local minima of the isotherm with  $T = T_0$  and  $p = 0$ . Only when  $T > T_0$ ,  $p > 0$  for all  $\nu > 1/3$ , so that the solution should satisfy the admissibility condition  $T > T_0$ . When  $T_c > T > T_0$ , see e.g. the isotherms where points A, B, and C are located, the states between the local minimum (at the point M with  $p_\nu = 0$ ) and the local maximum (at the point N with  $p_\nu = 0$ ) of  $p$  are unstable [44]. Due to the discriminant  $4T(T - 1) < 0$ , the equation  $p_\nu = 0$ , written as  $(\rho - 2)^3 - 3(\rho - 2) - 4T + 2 = 0$ , has three unequal real roots given explicitly by

$$\begin{aligned} \rho^* &= 2 \cos \left( \frac{\arccos(2T - 1)}{3} \right) + 2, & \rho^{**} &= 2 \cos \left( \frac{\arccos(2T - 1) + 2\pi}{3} \right) + 2, \\ \rho^{***} &= 2 \cos \left( \frac{\arccos(2T - 1) + 4\pi}{3} \right) + 2. \end{aligned}$$

For  $1 > 2T - 1 > 11/16$ , it is known that  $\arccos(2T - 1) \in (0, \pi/3)$ , so that one has

$$\cos\left(\frac{\arccos(2T - 1)}{3}\right) > \frac{1}{2},$$

which implies that  $\rho^* > 3$  is not an admissible state, and  $\rho^{**}$  and  $\rho^{***}$  are the densities at the points N and M, respectively, satisfying

$$\begin{aligned} 0 < \rho_N = \rho^{**} < 2 \cos\left(\frac{2\pi}{3}\right) + 2 = 1, \\ 1 = 2 \cos\left(\frac{4\pi}{3}\right) + 2 < \rho_M = \rho^{***} < 2 \cos\left(\frac{5\pi}{3}\right) + 2 = 3. \end{aligned}$$

Because  $p_\nu = 0$  should have two identical real roots for  $\nu > 1/3$  if  $T = T_c$ , one has  $\nu_N(T_c) = \nu_M(T_c) = \nu_D = 1$ , so that for  $T_c > T > T_0$ ,  $p_\nu < 0$  iff  $\nu > \nu_N$  or  $\nu < \nu_M$ . The left side of the point M corresponds to the liquid, while the right side of the point N is gas. Thus, the van der Waals gas should satisfy  $\nu > \nu_N$  when  $T_c > T > T_0$ . Lastly, by the way, a correction, see [44], may be made in the region  $p_\nu > 0$  with the help of Maxwell's assumption that the areas of the two parts enclosed by isotherms and isobars are equal. Specifically, for the isotherms where points A, B, and C are located, Using the equality of the two areas bounded by the isotherm and the isobar

$$\int_{\nu_A}^{\nu_B} \left( p - \frac{8T}{3\nu - 1} + \frac{3}{\nu^2} \right) d\nu = \int_{\nu_B}^{\nu_C} \left( \frac{8T}{3\nu - 1} - \frac{3}{\nu^2} - p \right) d\nu,$$

gives the expression of  $p$  depending on the unknowns  $\nu_A$  and  $\nu_C$ , which are the smallest and largest roots of the van der Waals equation, respectively. After that, the A-B-C segment is used to describe the state of the gas-liquid coexistence region.  $\square$

Now, let us recall the mathematical definition of the entropy function.

**Definition 2.1** (Entropy function). If associated with strictly convex scalar function  $\eta(\mathbf{U})$  there exist scalar functions  $q_k(\mathbf{U})$ ,  $k = 1, \dots, d$ , for the system (1.1) satisfying

$$q'_k(\mathbf{U}) = \eta'(\mathbf{U})^T \mathbf{F}'_k(\mathbf{U}), \quad k = 1, \dots, d,$$

then  $\eta$  and  $q_k$  are called the entropy function and the entropy fluxes, respectively, and  $(\eta, q_1, \dots, q_d)$  forms an entropy pair. The gradient vector of  $\eta$  with respect to  $\mathbf{U}$ , i.e.  $\mathbf{V} = \eta'(\mathbf{U})^T$ , is called the entropy variables.

Consider the scalar function pair for (1.1) taken as

$$\eta(\mathbf{U}) = -\rho s, \quad q_k(\mathbf{U}) = -\rho s v_k, \tag{2.5}$$

then one has

$$\mathbf{V} = \eta'(\mathbf{U})^T = \left( -s + \frac{1}{\delta} - \frac{|\mathbf{v}|^2}{2T} - \frac{9\rho}{4T} + \frac{3}{3-\rho}, \frac{\mathbf{v}^T}{T}, -\frac{1}{T} \right)^T,$$



and

$$\frac{\partial^2 \eta}{\partial \mathbf{U}^2} = \frac{\delta}{\rho T^2} \begin{bmatrix} \frac{T}{\delta} \left( \frac{9T}{(3-\rho)^2} - \frac{9}{4}\rho + |\mathbf{v}|^2 \right) + \left( \mu_\delta - \frac{T}{\delta} \right)^2 & -v_1 \mu_\delta & -v_2 \mu_\delta & -v_3 \mu_\delta & \mu_\delta - \frac{T}{\delta} \\ & -v_1 \mu_\delta & v_1^2 + \frac{T}{\delta} & v_1 v_2 & v_1 v_3 & -v_1 \\ & -v_2 \mu_\delta & v_2 v_1 & v_2^2 + \frac{T}{\delta} & v_2 v_3 & -v_2 \\ & -v_3 \mu_\delta & v_3 v_1 & v_3 v_2 & v_3^2 + \frac{T}{\delta} & -v_3 \\ & \mu_\delta - \frac{T}{\delta} & -v_1 & -v_2 & -v_3 & 1 \end{bmatrix}.$$

It can be verified that  $\frac{\partial^2 \eta}{\partial \mathbf{U}^2}$  is symmetric positive definite, so that  $(\eta, q_1, \dots, q_d)$  forms an entropy pair of (1.1). In this case, the entropy potential  $\phi$  and entropy flux potential  $\psi_k$  can be explicitly calculated by

$$\begin{aligned} \phi &= \mathbf{V}^T \mathbf{U} - \eta(\mathbf{U}) = - \left( \frac{9\rho}{8T} - \frac{3}{3-\rho} \right) \rho, \\ \psi_k &= \mathbf{V}^T \mathbf{F}_k(\mathbf{U}) - q_k(\mathbf{U}) = - \left( \frac{9\rho}{8T} - \frac{3}{3-\rho} \right) \rho v_k, \end{aligned} \quad (2.6)$$

and the system (1.1) may be symmetrized with the change of variables  $\mathbf{U} \mapsto \mathbf{V}$ , because that  $\frac{\partial \mathbf{U}}{\partial \mathbf{V}}$  is symmetric positive definite, and  $\frac{\partial \mathbf{F}_k}{\partial \mathbf{U}} \frac{\partial \mathbf{U}}{\partial \mathbf{V}}$  is symmetric, see Section 3.3.

Following [23], by a time dependent differentiable one-to-one coordinate mapping

$$t = \tau, \quad \mathbf{x} = \mathbf{x}(\boldsymbol{\xi}, \tau) \in \Omega_p, \quad \boldsymbol{\xi} = (\xi_1, \dots, \xi_d) \in \Omega_c, \quad (2.7)$$

where a reference mesh in the computational domain  $\Omega_c$  with coordinates  $\boldsymbol{\xi} = (\xi_1, \dots, \xi_d)$  can be viewed as the inverse image of the adaptive moving mesh in the physical domain  $\Omega_p$  with coordinates  $\mathbf{x} = (x_1, \dots, x_d)$ , the system (1.1) can be transformed into the following conservative form in curvilinear coordinates

$$\frac{\partial(J\mathbf{U})}{\partial \tau} + \sum_{k=1}^d \frac{\partial}{\partial \xi_k} \left[ \left( J \frac{\partial \xi_k}{\partial t} \mathbf{U} \right) + \sum_{j=1}^d \left( J \frac{\partial \xi_k}{\partial x_j} \mathbf{F}_j \right) \right] = 0, \quad J = \det \left( \frac{\partial(t, \mathbf{x})}{\partial(\tau, \boldsymbol{\xi})} \right). \quad (2.8)$$

Moreover, for the transformation (2.7), one should have the following geometric conservation laws (GCLs) including the volume conservation law (VCL) and the surface conservation laws (SCLs)

$$\begin{aligned} \text{VCL:} \quad & \frac{\partial J}{\partial \tau} + \sum_{k=1}^d \frac{\partial}{\partial \xi_k} \left( J \frac{\partial \xi_k}{\partial t} \right) = 0, \\ \text{SCLs:} \quad & \sum_{k=1}^d \frac{\partial}{\partial \xi_k} \left( J \frac{\partial \xi_k}{\partial x_j} \right) = 0, \quad j = 1, \dots, d, \end{aligned} \quad (2.9)$$

where the VCL indicates that the volumetric increment of a moving cell is equal to the sum of the changes along the surfaces that enclose the cell, while the SCLs imply that the cell volume should

be closed by its surfaces [62]. Utilizing (2.8) and the GCLs (2.9) as shown in [23], the entropy condition in curvilinear coordinates is given by

$$\frac{\partial(J\eta)}{\partial\tau} + \sum_{k=1}^d \frac{\partial}{\partial\xi_k} \left[ \left( J \frac{\partial\xi_k}{\partial t} \eta \right) + \sum_{j=1}^d \left( J \frac{\partial\xi_k}{\partial x_j} q_j \right) \right] \leq 0,$$

where the equality is established for the smooth solutions of (1.1), and the inequality holds for the discontinuous solutions in the sense of distributions.

### 3. Numerical schemes

This section presents the 3D adaptive moving mesh EC and ES finite difference schemes for the system (2.8) on the structured mesh, and the 1D and 2D schemes can be viewed as the degenerative case which is shown in the appendices in [23]. Dividing a cuboid computational domain  $\Omega_c : [a_1, b_1] \times [a_2, b_2] \times [a_3, b_3]$  into a fixed orthogonal uniform mesh  $\{(\xi_{1,i_1}, \xi_{2,i_2}, \xi_{3,i_3}) : a_k = \xi_{k,1} < \dots < \xi_{k,i_k} < \dots < \xi_{k,N_k} = b_k, k = 1, 2, 3\}$  with the constant mesh step size  $\Delta\xi_k = \xi_{k,i_k+1} - \xi_{k,i_k}$ , the semi-discrete conservative  $2w$ -order ( $w \geq 1$ ) finite difference schemes for (2.8) and the first equation in (2.9) are given by

$$\frac{d}{d\tau}(J\mathbf{U})_{\mathbf{i}} = - \sum_{k=1}^3 \frac{1}{\Delta\xi_k} \left( \left( \widehat{\mathbf{F}}_k \right)_{\mathbf{i},k,+\frac{1}{2}}^{2wth} - \left( \widehat{\mathbf{F}}_k \right)_{\mathbf{i},k,-\frac{1}{2}}^{2wth} \right), \quad (3.1)$$

$$\frac{d}{d\tau} J_{\mathbf{i}} = - \sum_{k=1}^3 \frac{1}{\Delta\xi_k} \left( \left( \widehat{J \frac{\partial\xi_k}{\partial t}} \right)_{\mathbf{i},k,+\frac{1}{2}}^{2wth} - \left( \widehat{J \frac{\partial\xi_k}{\partial t}} \right)_{\mathbf{i},k,-\frac{1}{2}}^{2wth} \right), \quad (3.2)$$

where the index  $\mathbf{i} = (i_1, i_2, i_3)$  denotes the point  $(\xi_{1,i_1}, \xi_{2,i_2}, \xi_{3,i_3})$ , the notation  $\{\mathbf{i}, k, m\}$  presents that the index  $\mathbf{i}$  increases  $m$  along  $i_k$ -direction, e.g.  $\{\mathbf{i}, 1, +\frac{1}{2}\}$  is  $(i_1 + \frac{1}{2}, i_2, i_3)$ ,  $J_{\mathbf{i}}(\tau)$  and  $(J\mathbf{U})_{\mathbf{i}}(\tau)$  approximate respectively the point values of  $J(\tau, \boldsymbol{\xi})$  and  $(J\mathbf{U})(\tau, \boldsymbol{\xi})$  at  $\mathbf{i}$ , and  $\left( \widehat{\mathbf{F}}_k \right)_{\mathbf{i},k,\pm\frac{1}{2}}^{2wth}$  and  $\left( \widehat{J \frac{\partial\xi_k}{\partial t}} \right)_{\mathbf{i},k,\pm\frac{1}{2}}^{2wth}$  are the numerical fluxes approximating respectively  $J \frac{\partial\xi_k}{\partial t} \mathbf{U} + \sum_{j=1}^3 J \frac{\partial\xi_k}{\partial x_j} \mathbf{F}_j$  and  $J \frac{\partial\xi_k}{\partial t}$  at  $\{\mathbf{i}, k, \pm\frac{1}{2}\}$ ,  $k = 1, 2, 3$ , see (3.12) and (3.13) in Section 3.1 for specific expressions. The SCLs (2.9) should also be satisfied in the discrete form

$$\sum_{k=1}^3 \frac{1}{\Delta\xi_k} \left( \left( \widehat{J \frac{\partial\xi_k}{\partial x_j}} \right)_{\mathbf{i},k,+\frac{1}{2}}^{2wth} - \left( \widehat{J \frac{\partial\xi_k}{\partial x_j}} \right)_{\mathbf{i},k,-\frac{1}{2}}^{2wth} \right) = 0, \quad j = 1, 2, 3, \quad (3.3)$$

where  $\left( \widehat{J \frac{\partial\xi_k}{\partial x_j}} \right)_{\mathbf{i},k,\pm\frac{1}{2}}^{2wth}$  is given by (3.13) in Section 3.1.

### 3.1. Two-point EC fluxes in curvilinear coordinates

This part proposes two-point symmetric EC fluxes in curvilinear coordinates according to the sufficient condition given in [23]. If a two-point symmetric flux  $\widehat{\mathbf{F}}_k \left( \mathbf{U}_l, \mathbf{U}_r, \left( J \frac{\partial \xi_k}{\partial \zeta} \right)_l, \left( J \frac{\partial \xi_k}{\partial \zeta} \right)_r \right)$ ,  $\zeta = t, x_1, x_2, x_3$  is consistent with  $J \frac{\partial \xi_k}{\partial t} \mathbf{U} + \sum_{j=1}^3 J \frac{\partial \xi_k}{\partial x_j} \mathbf{F}_j$ , chosen as

$$\begin{aligned} \widehat{\mathbf{F}}_k \left( \mathbf{U}_l, \mathbf{U}_r, \left( J \frac{\partial \xi_k}{\partial \zeta} \right)_l, \left( J \frac{\partial \xi_k}{\partial \zeta} \right)_r \right) &= \frac{1}{2} \left( \left( J \frac{\partial \xi_k}{\partial t} \right)_l + \left( J \frac{\partial \xi_k}{\partial t} \right)_r \right) \widetilde{\mathbf{U}} \\ &+ \sum_{j=1}^3 \frac{1}{2} \left( \left( J \frac{\partial \xi_k}{\partial x_j} \right)_l + \left( J \frac{\partial \xi_k}{\partial x_j} \right)_r \right) \widetilde{\mathbf{F}}_j, \end{aligned} \quad (3.4)$$

with  $\widetilde{\mathbf{U}} = \widetilde{\mathbf{U}}(\mathbf{U}_l, \mathbf{U}_r) = \widetilde{\mathbf{U}}(\mathbf{U}_r, \mathbf{U}_l)$  and  $\widetilde{\mathbf{F}}_j = \widetilde{\mathbf{F}}_j(\mathbf{U}_l, \mathbf{U}_r) = \widetilde{\mathbf{F}}_j(\mathbf{U}_r, \mathbf{U}_l)$  satisfying

$$(\mathbf{V}_r - \mathbf{V}_l)^T \widetilde{\mathbf{U}} = \phi(\mathbf{U}_r) - \phi(\mathbf{U}_l), \quad (\mathbf{V}_r - \mathbf{V}_l)^T \widetilde{\mathbf{F}}_j = \psi_j(\mathbf{U}_r) - \psi_j(\mathbf{U}_l), \quad (3.5)$$

then the semi-discrete scheme (3.1)-(3.2) is EC, that is, the solution satisfies the following semi-discrete entropy identity

$$\frac{d}{dt} J_i \eta(\mathbf{U}_i(t)) + \sum_{k=1}^3 \frac{1}{\Delta \xi_k} \left( (\widehat{q}_k)_{i,k,+\frac{1}{2}}^{2wth}(t) - (\widehat{q}_k)_{i,k,-\frac{1}{2}}^{2wth}(t) \right) = 0,$$

where  $\mathbf{U}_l$  and  $\mathbf{U}_r$  represent the left and right states, respectively, and the numerical entropy flux  $(\widehat{q}_k)_{i,k,+\frac{1}{2}}^{2wth}$  is consistent with the entropy flux  $J \frac{\partial \xi_k}{\partial t} \eta + \sum_{j=1}^3 J \frac{\partial \xi_k}{\partial x_j} q_j$  but it is not unique.

The explicit expressions of the two-point EC fluxes  $\widehat{\mathbf{F}}_k$  can be established under some admissible conditions. The notations

$$\{\{a\}\} = (a_r + a_l)/2, \quad \llbracket a \rrbracket = a_r - a_l,$$

are employed for convenience to denote respectively the arithmetic mean and jump of  $a$ , and choose the parameter vector as

$$\mathbf{z} = (z_1, z_2, z_3, z_4, z_5)^T = (\rho, \mathbf{v}^T, T)^T = \left( \rho, \mathbf{v}^T, \frac{(3-\rho)(p+3\rho^2)}{8\rho} \right)^T. \quad (3.6)$$

Using the identities

$$\llbracket ab \rrbracket = \{\{a\}\} \llbracket b \rrbracket + \llbracket b \rrbracket \{\{a\}\}, \quad \llbracket \frac{1}{b} \rrbracket = -\frac{\llbracket b \rrbracket}{b_l b_r}, \quad \llbracket \frac{a}{b} \rrbracket = \frac{\llbracket a \rrbracket}{\{\{b\}\}} - \{\{ \frac{a}{b} \} \} \frac{\llbracket b \rrbracket}{\{\{b\}\}},$$

gives the decomposition of  $\llbracket \mathbf{V} \rrbracket$  as follows

$$\left\{ \begin{array}{l} \llbracket \mathbf{V}_1 \rrbracket = \left( \frac{1}{\{\{z_1\}\}^{\ln}} + \frac{1}{\{\{3-z_1\}\}^{\ln}} + \frac{3}{(3-z_{1,L})(3-z_{1,R})} - \frac{9}{4\{\{z_5\}\}} \right) \llbracket z_1 \rrbracket \\ \quad + \left( \frac{1}{2} \sum_{m=2}^4 \frac{1}{\{\{z_5\}\}} \left\{ \frac{z_m^2}{z_5} \right\} - \frac{1}{\delta\{\{z_5\}\}^{\ln}} + \frac{9}{4} \frac{1}{\{\{z_5\}\}} \left\{ \frac{z_1}{z_5} \right\} \right) \llbracket z_5 \rrbracket - \sum_{m=2}^4 \frac{\{\{z_m\}\} \llbracket z_m \rrbracket}{\{\{z_5\}\}}, \\ \llbracket \mathbf{V}_m \rrbracket = -\frac{1}{\{\{z_5\}\}} \left\{ \frac{z_m}{z_5} \right\} \llbracket z_5 \rrbracket + \frac{1}{\{\{z_5\}\}} \llbracket z_m \rrbracket, \quad m = 2, 3, 4, \\ \llbracket \mathbf{V}_5 \rrbracket = \frac{1}{\{\{z_5\}\}} \left\{ \frac{1}{z_5} \right\} \llbracket z_5 \rrbracket, \end{array} \right. \quad (3.7)$$

where  $\{\{a\}\}^{\ln} := \llbracket a \rrbracket / \llbracket \ln a \rrbracket$ ,  $a > 0$  is the logarithmic mean, see [35]. Similarly,  $\llbracket \phi \rrbracket$  and  $\llbracket \psi_1 \rrbracket$  can be expanded as

$$\begin{aligned} \llbracket \phi \rrbracket &= \{\{z_1\}\} \left[ -\frac{9}{8} \frac{1}{\{\{z_5\}\}} \left( \llbracket z_1 \rrbracket - \left\{ \frac{z_1}{z_5} \right\} \llbracket z_5 \rrbracket \right) + \frac{3\llbracket z_1 \rrbracket}{(3-z_{1,L})(3-z_{1,R})} \right] + \llbracket z_1 \rrbracket \left\{ -\frac{9}{8} \frac{z_1}{z_5} + \frac{3}{3-z_1} \right\} \\ &= \left[ \{\{z_1\}\} \left( -\frac{9}{8} \frac{1}{\{\{z_5\}\}} + \frac{3}{(3-z_{1,L})(3-z_{1,R})} \right) + \left\{ -\frac{9}{8} \frac{z_1}{z_5} + \frac{3}{3-z_1} \right\} \right] \llbracket z_1 \rrbracket \\ &\quad + \frac{9}{8} \frac{\{\{z_1\}\}}{\{\{z_5\}\}} \left\{ \frac{z_1}{z_5} \right\} \llbracket z_5 \rrbracket, \\ \llbracket \psi_1 \rrbracket &= \{\{z_1 z_2\}\} \left[ -\frac{9}{8} \frac{1}{\{\{z_5\}\}} \left( \llbracket z_1 \rrbracket - \left\{ \frac{z_1}{z_5} \right\} \llbracket z_5 \rrbracket \right) + \frac{3\llbracket z_1 \rrbracket}{(3-z_{1,L})(3-z_{1,R})} \right] \\ &\quad + (\llbracket z_1 \rrbracket \{\{z_2\}\} + \llbracket z_2 \rrbracket \{\{z_1\}\}) \left\{ -\frac{9}{8} \frac{z_1}{z_5} + \frac{3}{3-z_1} \right\} \\ &= \left[ \{\{z_1 z_2\}\} \left( -\frac{9}{8} \frac{1}{\{\{z_5\}\}} + \frac{3}{(3-z_{1,L})(3-z_{1,R})} \right) + \left\{ -\frac{9}{8} \frac{z_1}{z_5} + \frac{3}{3-z_1} \right\} \{\{z_2\}\} \right] \llbracket z_1 \rrbracket \\ &\quad + \frac{9}{8\{\{z_5\}\}} \{\{z_1 z_2\}\} \left\{ \frac{z_1}{z_5} \right\} \llbracket z_5 \rrbracket + \{\{z_1\}\} \left\{ -\frac{9}{8} \frac{z_1}{z_5} + \frac{3}{3-z_1} \right\} \llbracket z_2 \rrbracket. \end{aligned}$$

Substituting (3.7) and the above identities into two identities in (3.5) for the two-point EC fluxes and equating the coefficients of the same jump terms on both side of the identities derive

$$\left\{ \begin{array}{l} \left( \frac{1}{\{\{z_1\}\}^{\ln}} + \frac{1}{\{\{3-z_1\}\}^{\ln}} + \frac{3}{(3-z_{1,L})(3-z_{1,R})} - \frac{9}{4\{\{z_5\}\}} \right) \tilde{\mathbf{U}}_1 \\ = \left( \{\{z_1\}\} \left( -\frac{9}{8} \frac{1}{\{\{z_5\}\}} + \frac{3}{(3-z_{1,L})(3-z_{1,R})} \right) + \left\{ -\frac{9}{8} \frac{z_1}{z_5} + \frac{3}{3-z_1} \right\} \right), \\ -\frac{1}{\{\{z_5\}\}} \{\{z_m\}\} \tilde{\mathbf{U}}_1 + \frac{1}{\{\{z_5\}\}} \tilde{\mathbf{U}}_m = 0, \quad m = 2, 3, 4, \\ \left( \frac{1}{2} \sum_{m=2}^4 \frac{1}{\{\{z_5\}\}} \left\{ \frac{z_m^2}{z_5} \right\} - \frac{1}{\delta\{\{z_5\}\}^{\ln}} + \frac{9}{4} \frac{1}{\{\{z_5\}\}} \left\{ \frac{z_1}{z_5} \right\} \right) \tilde{\mathbf{U}}_1 - \sum_{m=2}^4 \frac{1}{\{\{z_5\}\}} \left\{ \frac{z_m}{z_5} \right\} \tilde{\mathbf{U}}_m \\ + \frac{1}{\{\{z_5\}\}} \left\{ \frac{1}{z_5} \right\} \tilde{\mathbf{U}}_5 = \frac{9}{8} \frac{\{\{z_1\}\}}{\{\{z_5\}\}} \left\{ \frac{z_1}{z_5} \right\}, \end{array} \right. \quad (3.8)$$

$$\left\{ \begin{array}{l}
\left( \frac{1}{\{\{z_1\}\}^{\ln}} + \frac{1}{\{\{3-z_1\}\}^{\ln}} + \frac{3}{(3-z_{1,L})(3-z_{1,R})} - \frac{9}{4\{\{z_5\}\}} \right) \tilde{\mathbf{F}}_{1,1} \\
= \{\{z_1 z_2\}\} \left( -\frac{9}{8} \frac{1}{\{\{z_5\}\}} + \frac{3}{(3-z_{1,L})(3-z_{1,R})} \right) + \left\{ \left\{ -\frac{9}{8} \frac{z_1}{z_5} + \frac{3}{3-z_1} \right\} \right) \{\{z_2\}\}, \\
-\frac{1}{\{\{z_5\}\}} \{\{z_2\}\} \tilde{\mathbf{F}}_{1,1} + \frac{1}{\{\{z_5\}\}} \tilde{\mathbf{F}}_{1,2} = \{\{z_1\}\} \left\{ \left\{ -\frac{9}{8} \frac{z_1}{z_5} + \frac{3}{3-z_1} \right\} \right), \\
-\frac{1}{\{\{z_5\}\}} \{\{z_m\}\} \tilde{\mathbf{F}}_{1,1} + \frac{1}{\{\{z_5\}\}} \tilde{\mathbf{F}}_{1,m} = 0, \quad m = 3, 4, \\
\left( \frac{1}{2} \sum_{m=2}^4 \frac{1}{\{\{z_5\}\}} \left\{ \frac{z_m^2}{z_5} \right\} - \frac{1}{\delta \{\{z_5\}\}^{\ln}} + \frac{9}{4} \frac{1}{\{\{z_5\}\}} \left\{ \frac{z_1}{z_5} \right\} \right) \tilde{\mathbf{F}}_{1,1} - \sum_{m=2}^4 \frac{1}{\{\{z_5\}\}} \left\{ \frac{z_m}{z_5} \right\} \tilde{\mathbf{F}}_{1,m} \\
+ \frac{1}{\{\{z_5\}\}} \left\{ \frac{1}{z_5} \right\} \tilde{\mathbf{F}}_{1,5} = \frac{9\{\{z_1 z_2\}\}}{8\{\{z_5\}\}} \left\{ \frac{z_1}{z_5} \right\}.
\end{array} \right. \quad (3.9)$$

**Theorem 3.1.** Assuming that  $z_l, z_r$  satisfy the constraints in Remark 2.1 and  $\{\{z\}\}$  satisfies

$$4\{\{z_5\}\} - \{\{z_1\}\} (3 - \{\{z_1\}\})^2 > 0, \quad (3.10)$$

the linear equations (3.8)-(3.9) have a unique solution.

*Proof.* According to Remark 2.1, one can easily deduce

$$3 > \{\{z_1\}\} > 0, \quad \{\{z_5\}\} > \frac{27}{32} > 0, \quad \left\{ \frac{1}{z_5} \right\} = \frac{z_{5,l} + z_{5,r}}{2z_{5,l}z_{5,r}} > 0. \quad (3.11)$$

The determinant of the coefficient matrix of the linear equations (3.8)-(3.9) is  $D \frac{2}{\{\{z_5\}\}^4} \left\{ \frac{1}{z_5} \right\}$  with

$$D := \frac{1}{\{\{z_1\}\}^{\ln}} + \frac{1}{\{\{3-z_1\}\}^{\ln}} + \frac{3}{(3-z_{1,l})(3-z_{1,r})} - \frac{9}{4\{\{z_5\}\}}.$$

The system (3.8)-(3.9) has a unique solution only if the determinant of the coefficient matrix is not equal to zero, i.e  $D \neq 0$ , based on the conditions (3.11). Because  $3 > \{\{z_1\}\} > 0$ ,  $\{\{z_1\}\}^{\ln}$  and  $\{\{3-z_1\}\}^{\ln}$  are well-defined. Using  $\{\{z_1\}\} \geq \{\{z_1\}\}^{\ln} > 0$ ,  $\{\{3-z_1\}\} \geq \{\{3-z_1\}\}^{\ln} > 0$ ,  $\{\{3-z_1\}\}^2 \geq (3-z_{1,l})(3-z_{1,r}) > 0$  and the constraints (3.10) can derive the following inequality

$$\begin{aligned}
D &\geq \frac{1}{\{\{z_1\}\}} + \frac{1}{\{\{3-z_1\}\}} + \frac{3}{\{\{3-z_1\}\}^2} - \frac{9}{4\{\{z_5\}\}} \\
&= \frac{9}{\{\{z_1\}\}\{\{3-z_1\}\}^2} - \frac{9}{4\{\{z_5\}\}} \\
&= \frac{9}{4\{\{z_1\}\}\{\{3-z_1\}\}^2\{\{z_5\}\}} (4\{\{z_5\}\} - \{\{z_1\}\}\{\{3-z_1\}\}^2) > 0.
\end{aligned}$$

Then the proof is completed.  $\square$

**Remark 3.1.** If  $z_l, z_r$  satisfy the conditions in Remark 2.1 and  $\{\{z_5\}\} = \{\{T\}\} > T_c$ , the inequality (3.10) is obviously satisfied since  $f(\{\{z_1\}\}) = \{\{z_1\}\}(3 - \{\{z_1\}\})^2$ ,  $\{\{z_1\}\} \in (0, 3)$  achieves the maximum 4 at  $\{\{z_1\}\} = 1$ .  $\square$

**Remark 3.2.** Because the van der Waals EOS is only used to describe van der Waals gas in this paper,  $\nu > \nu_N$  if  $T_0 < T < T_c$ , as shown in Figure 2.1. Thus, when  $T_0 < \{\{T\}\} = T_l = T_r < T_c$  and  $z_l, z_r$  satisfy the constraints in Remark 2.1,  $\rho_l < 1/\nu_N(\{\{T\}\})$  and  $\rho_r < 1/\nu_N(\{\{T\}\})$ , so that  $\{\{\rho\}\} < 1/\nu_N(\{\{T\}\})$ , i.e. the inequality (3.10) is satisfied. The numerical tests used in Section 5 are consistent with the conditions given by the Theorem 3.1.  $\square$

One can also similarly obtain different linear systems about  $\tilde{\mathbf{U}}$  and  $\tilde{\mathbf{F}}_1$  by using other parameter vectors, which are shown in Appendix A. However, the existence and uniqueness of the linear system about  $\tilde{\mathbf{U}}$  and  $\tilde{\mathbf{F}}_1$  is the critical factor to deduce the explicit expression of the two-point symmetric EC flux, which is not trivial for the compressible Euler equations with the van der Waals EOS. Under the conditions given by Theorem 3.1, the system (3.8)-(3.9) has a unique solution, and the explicit expressions of the solutions  $\tilde{\mathbf{U}}$  and  $\tilde{\mathbf{F}}_1$  are given as follows

$$\left\{ \begin{array}{l} \tilde{\mathbf{U}}_1 = \frac{\{\{z_1\}\} \left( -\frac{9}{8} \frac{1}{\{\{z_5\}\}} + \frac{3}{(3-z_{1,L})(3-z_{1,R})} \right) + \left\{ \left\{ -\frac{9z_1}{8z_5} + \frac{3}{3-z_1} \right\} \right)}{\frac{1}{\{\{z_1\}\}^{\ln}} + \frac{1}{\{\{3-z_1\}\}^{\ln}} + \frac{3}{(3-z_{1,L})(3-z_{1,R})} - \frac{9}{4\{\{z_5\}\}}}, \\ \tilde{\mathbf{U}}_m = \{\{z_m\}\} \tilde{\mathbf{U}}_1, \quad m = 2, 3, 4, \\ \tilde{\mathbf{U}}_5 = \frac{1}{\{\{1/z_5\}\}} \left( -\left( \frac{1}{2} \sum_{m=2}^4 \{\{z_m^2\}\} - \frac{\{\{z_5\}\}}{\delta\{\{z_5\}\}^{\ln}} + \frac{9}{4} \{\{z_1\}\} \right) \tilde{\mathbf{U}}_1 + \sum_{m=2}^4 \{\{z_m\}\} \tilde{\mathbf{U}}_m + \frac{9}{8} \{\{z_1\}\} \{\{z_5\}\} \right), \\ \tilde{\mathbf{F}}_{1,1} = \frac{\{\{z_1 z_2\}\} \left( -\frac{9}{8} \frac{1}{\{\{z_5\}\}} + \frac{3}{(3-z_{1,L})(3-z_{1,R})} \right) + \left\{ \left\{ -\frac{9z_1}{8z_5} + \frac{3}{3-z_1} \right\} \{\{z_2\}\} \right)}{\frac{1}{\{\{z_1\}\}^{\ln}} + \frac{1}{\{\{3-z_1\}\}^{\ln}} + \frac{3}{(3-z_{1,L})(3-z_{1,R})} - \frac{9}{4\{\{z_5\}\}}}, \\ \tilde{\mathbf{F}}_{1,2} = \{\{z_1\}\} \{\{z_5\}\} \left\{ \left\{ -\frac{9z_1}{8z_5} + \frac{3}{3-z_1} \right\} \right\} + \{\{z_2\}\} \tilde{\mathbf{F}}_{1,1}, \\ \tilde{\mathbf{F}}_{1,m} = \{\{z_m\}\} \tilde{\mathbf{F}}_{1,1}, \quad m = 3, 4, \\ \tilde{\mathbf{F}}_{1,5} = \frac{1}{\{\{1/z_5\}\}} \left( -\left( \frac{1}{2} \sum_{m=2}^4 \{\{z_m^2\}\} - \frac{\{\{z_5\}\}}{\delta\{\{z_5\}\}^{\ln}} + \frac{9}{4} \{\{z_1\}\} \right) \tilde{\mathbf{F}}_{1,1} + \sum_{m=2}^4 \{\{z_m\}\} \tilde{\mathbf{F}}_{1,m} + \frac{9\{\{z_1 z_2\}\}}{8} \{\{z_5\}\} \right). \end{array} \right.$$

Similarly,  $\tilde{\mathbf{F}}_k$  may be derived for  $k = 2, 3$ .

**Remark 3.3.** It can be easily verified that the above two-point EC flux is consistent with  $J \frac{\partial \xi_k}{\partial t} \mathbf{U} + \sum_{j=1}^3 J \frac{\partial \xi_k}{\partial x_j} \mathbf{F}_j$  by proving  $\tilde{\mathbf{U}}$  and  $\tilde{\mathbf{F}}_k$  are consistent with  $\mathbf{U}$  and  $\mathbf{F}_k$ , respectively. If  $(\rho_l, \mathbf{v}_l^T, p_l)^T = (\rho_r, \mathbf{v}_r^T, p_r)^T = (\rho, \mathbf{v}^T, p)^T$ , then

$$\tilde{\mathbf{F}}_{1,1} = \frac{\rho v_1 \left( -\frac{9\rho}{(p+3\rho^2)(3-\rho)} + \frac{3}{(3-\rho)^2} \right) + \left( -\frac{9\rho}{(p+3\rho^2)(3-\rho)} \rho + \frac{3}{(3-\rho)} \right) v_1}{\frac{1}{\rho} + \frac{1}{3-\rho} + \frac{3}{(3-\rho)^2} - \frac{18\rho}{(p+3\rho^2)(3-\rho)}}$$

$$\begin{aligned}
&= \frac{\rho v_1 \left( -\frac{18\rho}{(p+3\rho^2)(3-\rho)} + \frac{3}{(3-\rho)^2} \right) + \frac{3v_1}{(3-\rho)}}{-\frac{18\rho}{(p+3\rho^2)(3-\rho)} + \frac{3}{\rho(3-\rho)}} = \rho v_1 = \mathbf{F}_{1,1}, \\
\tilde{\mathbf{F}}_{1,2} &= \frac{(p+3\rho^2)(3-\rho)}{8} \left( -\frac{9\rho^2}{(p+3\rho^2)(3-\rho)} + \frac{3}{3-\rho} \right) + \rho v_1^2 = \rho v_1^2 + \frac{3}{8}p = \mathbf{F}_{1,2}, \\
\tilde{\mathbf{F}}_{1,3} &= \rho v_1 v_2 = \mathbf{F}_{1,3}, \quad \tilde{\mathbf{F}}_{1,4} = \rho v_1 v_3 = \mathbf{F}_{1,4}, \\
\tilde{\mathbf{F}}_{1,5} &= \left( -\frac{1}{2}|\mathbf{v}|^2 + \frac{(3-\rho)(p+3\rho^2)}{8\delta\rho} - \frac{9}{4}\rho \right) \rho v_1 + v_1 \left( \rho|\mathbf{v}|^2 + \frac{3}{8}p \right) + \frac{9}{8}\rho^2 v_1 = v_1 \left( E + \frac{3}{8}p \right) = \mathbf{F}_{1,5},
\end{aligned}$$

and the consistency of  $\tilde{\mathbf{U}}$  and  $\tilde{\mathbf{F}}_k, k = 2, 3$ , can be similarly deduced.  $\square$

Using the linear combination of the two point EC fluxes (3.4), the semi-discrete  $2w$ th-order EC schemes (3.1)-(3.2) can be constructed with the following  $2w$ th-order EC fluxes according to [23]

$$\left( \widehat{\mathbf{F}}_k \right)_{i,k,+\frac{1}{2}}^{2w\text{th}} = \sum_{m=1}^w \alpha_{w,m} \sum_{s=0}^{m-1} \widehat{\mathbf{F}}_k \left( \mathbf{U}_{i,k,-s}, \mathbf{U}_{i,k,-s+m}, \left( J \frac{\partial \xi_k}{\partial \zeta} \right)_{i,k,-s}, \left( J \frac{\partial \xi_k}{\partial \zeta} \right)_{i,k,-s+m} \right), \quad (3.12)$$

$$\left( \widehat{J \frac{\partial \xi_k}{\partial \zeta}} \right)_{i,k,+\frac{1}{2}}^{2w\text{th}} = \sum_{m=1}^w \alpha_{w,m} \sum_{s=0}^{m-1} \frac{1}{2} \left( \left( J \frac{\partial \xi_k}{\partial \zeta} \right)_{i,k,-s} + \left( J \frac{\partial \xi_k}{\partial \zeta} \right)_{i,k,-s+m} \right), \quad \zeta = t, x_1, x_2, x_3, \quad (3.13)$$

where the constants  $\{\alpha_{w,m}\}$  satisfy the following conditions [37]

$$\sum_{m=1}^w m \alpha_{w,m} = 1, \quad \sum_{m=1}^w m^{2s-1} \alpha_{w,m} = 0, \quad s = 2, \dots, w.$$

### 3.2. Discrete GCLs

This section constructs the discrete GCLs, which need to be fulfilled, otherwise they may lead to a misrepresentation of the convective velocities and extra sources or sinks in the physically conservative media [62]. Moreover, the discrete GCLs play an important role in constructing the semi-discrete EC/ES schemes (3.1)-(3.2) satisfying the semi-discrete entropy conditions. Utilizing the  $2w$ th-order accurate discretizations for  $J \frac{\partial \xi_k}{\partial x_j}$ ,  $k, j = 1, 2, 3$ , given in [23], for example,

$$\left( J \frac{\partial \xi_1}{\partial x_1} \right)_i = \left( \frac{\partial x_2}{\partial \xi_2} \frac{\partial x_3}{\partial \xi_3} - \frac{\partial x_2}{\partial \xi_3} \frac{\partial x_3}{\partial \xi_2} \right)_i = \frac{1}{\Delta \xi_2 \Delta \xi_3} (\delta_3 [\delta_2 [x_2] x_3] - \delta_2 [\delta_3 [x_2] x_3])_i, \quad (3.14)$$

with the  $2w$ th-order central difference operator in the  $\xi_k$ -direction

$$\delta_k [a_i] = \frac{1}{2} \sum_{m=1}^w \alpha_{w,m} (a_{i,k,+m} - a_{i,k,-m}).$$

and combining (3.14) with the  $2w$ th-order discretizations of the fluxes in (3.13) can easily obtain the discrete SCLs (3.3).

Due to the transformation (2.7), the metrics  $J \frac{\partial \xi_k}{\partial t}$  can be efficiently approximated by

$$\left( J \frac{\partial \xi_k}{\partial t} \right)_i = - \sum_{j=1}^3 (\dot{x}_j)_i \left( J \frac{\partial \xi_k}{\partial x_j} \right)_i, \quad k = 1, 2, 3, \quad (3.15)$$

with  $\left( J \frac{\partial \xi_k}{\partial x_j} \right)_i$  calculated by (3.14), and the mesh velocities  $(\dot{x}_j)_i$ ,  $j = 1, 2, 3$ , determined by the adaptive moving mesh strategy shown in Section 4. Combining them with the fluxes (3.13) can obtain the high-order semi-discrete VCL (3.2).

At the end of this section, the steps of deriving the  $2w$ th-order semi-discrete EC scheme (3.1)-(3.2) in curvilinear coordinates are summarized as follows.

1. The two-point EC flux (3.4) in curvilinear coordinates is first explicitly derived based on the given entropy pair and carefully chosen parameter vector.
2. Construct the  $2w$ th-order accurate discretizations for  $\left( J \frac{\partial \xi_k}{\partial x_j} \right)_i$  using (3.14) so that the discrete SCLs hold. Combining  $\left( J \frac{\partial \xi_k}{\partial x_j} \right)_i$  with the mesh velocities  $(\dot{x}_j)_i$ , the  $2w$ th-order accurate discretizations for  $\left( J \frac{\partial \xi_k}{\partial t} \right)_i$  are given by (3.15).
3. Compute  $\left( \widehat{J \frac{\partial \xi_k}{\partial \zeta}} \right)_{i,k,+\frac{1}{2}}^{2w\text{th}}$  by using the linear combinations (3.13), which can get  $2w$ th-order accurate semi-discrete VCL, and similarly obtain the  $2w$ th-order accurate EC flux  $\left( \widehat{\mathbf{F}}_k \right)_{i,k,+\frac{1}{2}}^{2w\text{th}}$  by combining with the linear combination of two-point EC flux (3.12).

### 3.3. ES schemes

For the quasi-linear hyperbolic conservation laws, the entropy identity holds only when the solution is smooth, implying that EC schemes work well only for smooth solutions.

In order to capture the discontinuous solutions and to suppress the numerical oscillations which may produce by the EC schemes near the discontinuities, the high-order accurate ES schemes satisfied the semi-discrete entropy inequality for the given entropy pair should be constructed. Following [23], the following flux given by adding suitable dissipation term to the EC flux is ES

$$\left( \widehat{\mathbf{F}}_k \right)_{i,k,+\frac{1}{2}}^{\nu\text{th}} = \left( \widehat{\mathbf{F}}_k \right)_{i,k,+\frac{1}{2}}^{2w\text{th}} - \frac{1}{2} (\Lambda \mathbf{T}^{-1} \mathbf{R}(\mathbf{T}\mathbf{U}) \mathbf{Y})_{i,k,+\frac{1}{2}} \llbracket \mathbf{W} \rrbracket_{i,k,+\frac{1}{2}}^{\text{WENOMR}}, \quad (3.16)$$

where  $\Lambda := \max_m \left\{ \left| J \frac{\partial \xi_k}{\partial t} + L_k \lambda_m(\mathbf{T}\mathbf{U}) \right| \right\}$  with  $L_k = \sqrt{\sum_{j=1}^3 \left( J \frac{\partial \xi_k}{\partial x_j} \right)^2}$ ,  $\lambda_m$  is the eigenvalues of the



matrix  $\frac{\partial \mathbf{F}_1}{\partial \mathbf{U}}$ , the rotational matrix  $\mathbf{T}$  is defined by

$$\mathbf{T} = \begin{bmatrix} 1 & 0 & 0 & 0 & 0 \\ 0 & \cos \varphi \cos \theta & \cos \varphi \sin \theta & \sin \varphi & 0 \\ 0 & -\sin \theta & \cos \theta & 0 & 0 \\ 0 & -\sin \varphi \cos \theta & -\sin \varphi \sin \theta & \cos \varphi & 0 \\ 0 & 0 & 0 & 0 & 1 \end{bmatrix},$$

$$\theta = \arctan \left( \left( J \frac{\partial \xi_k}{\partial x_2} \right) / \left( J \frac{\partial \xi_k}{\partial x_1} \right) \right),$$

$$\varphi = \arctan \left( \left( J \frac{\partial \xi_k}{\partial x_3} \right) / \sqrt{\left( J \frac{\partial \xi_k}{\partial x_1} \right)^2 + \left( J \frac{\partial \xi_k}{\partial x_2} \right)^2} \right),$$

and  $\mathbf{R}$  is the scaled right eigenvector matrix corresponding to  $\frac{\partial \mathbf{F}_1}{\partial \mathbf{U}}$ , satisfying

$$\frac{\partial \mathbf{U}}{\partial \mathbf{V}} = \mathbf{R} \mathbf{R}^T, \quad \frac{\partial \mathbf{F}_1}{\partial \mathbf{U}} = \mathbf{R} \mathbf{\Lambda} \mathbf{R}^{-1}. \quad (3.17)$$

Let us derive the explicit expression of  $\mathbf{R}$ . The Jacobian  $\frac{\partial \mathbf{F}_1}{\partial \mathbf{U}}$  is given as follows

$$\begin{bmatrix} 0 & 1 & 0 & 0 & 0 \\ c_s^2 - v_1^2 - \frac{3p_e}{8\rho}(H - |\mathbf{v}|^2) & 2v_1 - \frac{3p_e}{8\rho}v_1 & -\frac{3p_e}{8\rho}v_2 & -\frac{3p_e}{8\rho}v_3 & \frac{3p_e}{8\rho} \\ -v_1v_2 & v_2 & v_1 & 0 & 0 \\ -v_1v_3 & v_3 & 0 & v_1 & 0 \\ v_1(c_s^2 - H) - \frac{3p_e}{8\rho}v_1(H - |\mathbf{v}|^2) & H - v_1^2 \frac{3p_e}{8\rho} & -\frac{3p_e}{8\rho}v_1v_2 & -\frac{3p_e}{8\rho}v_1v_3 & v_1 + \frac{3p_e}{8\rho}v_1 \end{bmatrix},$$

where  $H = (E + 3/8\rho)/\rho$  is the total enthalpy, and  $p_e$  denotes the partial derivative of  $p(\rho, e)$  with respect to  $e$ , i.e.  $p_e = \frac{8\delta\rho}{3 - \rho}$ . The eigenvalues  $\lambda_m, m = 1, \dots, 5$  of matrix  $\frac{\partial \mathbf{F}_1}{\partial \mathbf{U}}$  are given by

$$\{v_1 - c_s, v_1, v_1, v_1, v_1 + c_s\},$$

and the right eigenvector matrix

$$\tilde{\mathbf{R}}_1 = \begin{bmatrix} 1 & 1 & 0 & 0 & 1 \\ v_1 - c_s & v_1 & 0 & 0 & v_1 + c_s \\ v_2 & v_2 & 1 & 0 & v_2 \\ v_3 & v_3 & 0 & 1 & v_3 \\ H - v_1c_s & H - \frac{8c_s^2\rho}{3p_e} & v_2 & v_3 & H + v_1c_s \end{bmatrix},$$

satisfies  $\frac{\partial \mathbf{U}}{\partial \mathbf{V}} = \mathbf{R} \mathbf{R}^T = \tilde{\mathbf{R}}_1 \mathbf{S} \mathbf{S}^T \tilde{\mathbf{R}}_1^T$  with the diagonal matrix  $\mathbf{S}$ . Under the assumption that the numerical solution satisfies the conditions in Remark (2.1),  $\mathbf{S}$  can be expressed after calculation as

follows

$$\begin{bmatrix} \frac{\rho T}{2c_s^2} & 0 & 0 & 0 & 0 \\ 0 & \frac{4\delta\rho T^2}{(4T - \rho(3 - \rho)^2)c_s^2} & 0 & 0 & 0 \\ 0 & 0 & \rho T & 0 & 0 \\ 0 & 0 & 0 & \rho T & 0 \\ 0 & 0 & 0 & 0 & \frac{\rho T}{2c_s^2} \end{bmatrix}^{\frac{1}{2}},$$

so that the scaled right eigenvector matrix  $\mathbf{R}$  may be taken as  $\tilde{\mathbf{R}}\mathbf{S}$ . The values of  $\mathbf{R}_{i,k,+\frac{1}{2}}$  and  $\Lambda_{i,k,+\frac{1}{2}}$  are calculated by some averaged values of the primitive variables in the numerical tests such as

$$\bar{\rho} = \{\{\rho\}\}_{i,k,+\frac{1}{2}}^{\ln}, \quad \bar{v} = \{\{v\}\}_{i,k,+\frac{1}{2}}, \quad \bar{p} = \left( \frac{\{\{\rho\}\}^{\ln}}{\{\{\rho/p\}\}^{\ln}} \right)_{i,k,+\frac{1}{2}}.$$

To achieve high-order accuracy, the fifth-order multi-resolution WENO reconstruction [58] is applied to the scaled entropy variables  $\mathbf{W} = \mathbf{R}^T(\mathbf{TU})\mathbf{TV}$  to obtain the left and right limit values  $\mathbf{W}_{i,k,+\frac{1}{2}}^{\text{WENOMR},-}$  and  $\mathbf{W}_{i,k,+\frac{1}{2}}^{\text{WENOMR},+}$  in the jump terms  $\llbracket \mathbf{W} \rrbracket_{i,k,+\frac{1}{2}}^{\text{WENOMR}} := \mathbf{W}_{i,k,+\frac{1}{2}}^{\text{WENOMR},+} - \mathbf{W}_{i,k,+\frac{1}{2}}^{\text{WENOMR},-}$  in (3.16). Due to the fact that multi-resolution WENO reconstruction may not preserve the ‘‘sign’’ property proposed in [6], the diagonal matrix  $\mathbf{Y}_{i,k,+\frac{1}{2}}$  is chosen as the following form

$$(\mathbf{Y}_{m,m})_{i,k,+\frac{1}{2}} = \begin{cases} 1, & \text{if } \text{sign} \left( \llbracket \mathbf{W}_m \rrbracket_{i,k,+\frac{1}{2}}^{\text{WENOMR}} \right) \text{sign} \left( \llbracket \mathbf{W}_m \rrbracket_{i,k,+\frac{1}{2}} \right) > 0, \\ 0, & \text{otherwise,} \end{cases}$$

to make sure the flux given in (3.16) is ES.

**Remark 3.4.** The free-stream condition (if the initial value is constant, so is the solution of the numerical scheme at following instant) is an important property that should be met to prevent large errors and even numerical instabilities [55]. According to [23], it is easy to prove that our high-order accurate fully-discrete adaptive moving mesh EC/ES finite difference schemes satisfy the free-stream condition with the third-order accurate explicit SSP-RK schemes [28] for time discretization.  $\square$

#### 4. Adaptive moving mesh strategy

This section introduces briefly the adaptive moving mesh strategy mentioned in [23] for integrity, and especially concentrates on the selection of monitor function which decides the way how mesh clusters. Unless otherwise stated, the dependence of the variables on  $t = \tau$  from transformation (2.7) will be omitted. Following the Winslow variable diffusion method [59], the adaptive mesh

redistribution is implemented by iteratively solving the Euler-Lagrange equations of mesh adaption functional

$$\nabla_{\boldsymbol{\xi}} \cdot (\omega \nabla_{\boldsymbol{\xi}} x_k) = 0, \quad \boldsymbol{\xi} \in \Omega_c, \quad k = 1, 2, 3, \quad (4.1)$$

where the positive monitor function  $\omega$  is related to some physical variables controlling the location of the mesh points, taken as

$$\omega = \left( 1 + \sum_{k=1}^{\kappa} \alpha_k \frac{|\nabla_{\boldsymbol{\xi}} \delta_k|^2}{\max |\nabla_{\boldsymbol{\xi}} \delta_k|^2} + \alpha_{\kappa+1} \frac{|\Delta_{\boldsymbol{\xi}} G|^2}{\max |\Delta_{\boldsymbol{\xi}} G|^2} \right)^{1/2}, \quad (4.2)$$

with the positive constant parameter  $\alpha_k$ , the physical variable  $\delta_k$ , the number of physical variables  $\kappa$ , and the vector  $\left( \frac{\partial^2 a}{\partial \xi_1^2}, \dots, \frac{\partial^2 a}{\partial \xi_d^2} \right)$  denoted by  $\Delta_{\boldsymbol{\xi}} a$  in this paper. The appearance of the non-classical waves is often related to the sign of the fundamental derivative  $G$ , see Example 5.2. Therefore, for the van der Waals gas, the fundamental derivative  $G$  should be considered in the construction of  $\omega$  to enhance the capability of capturing non-classical waves. Using the second-order central difference scheme and the Jacobi iteration method, the mesh equations (4.1) are approximated by

$$\sum_{k=1}^d \left[ \omega_{i,k,+\frac{1}{2}} \left( \mathbf{x}_{i,k,1}^{[\nu]} - \mathbf{x}_i^{[\nu+1]} \right) - \omega_{i,k,-\frac{1}{2}} \left( \mathbf{x}_i^{[\nu+1]} - \mathbf{x}_{i,k,-1}^{[\nu]} \right) \right] / \Delta \xi_k^2 = 0, \quad \nu = 0, 1, \dots, \mu,$$

where  $\mathbf{x}_i^{[0]} := \mathbf{x}_i^n$ , and  $\omega_{i,k,\pm\frac{1}{2}} := \frac{1}{2} (\omega_{i,k} + \omega_{i,k,\pm 1})$ . The iteration stops when  $|\mathbf{x}^{[\nu]} - \mathbf{x}^{[\nu+1]}| < \epsilon$  or  $\nu > \mu$ , where  $\epsilon$  is the tolerable error. The total iteration number  $\mu$  is taken as 10 in our numerical tests, unless otherwise stated. Moreover, the following low pass filter

$$\omega_{i_1, i_2, i_3} \leftarrow \sum_{j_1, j_2, j_3=0, \pm 1} \left( \frac{1}{2} \right)^{|j_1|+|j_2|+|j_3|+3} \omega_{i_1+j_1, i_2+j_2, i_3+j_3},$$

is used to smooth monitor function 3 ~ 10 times in this work.

The final adaptive mesh at  $t^{n+1}$  is obtained with the limiter of the movement of mesh points  $\Delta_{\gamma}$  as follows

$$\begin{aligned} \mathbf{x}_i^{n+1} &:= \mathbf{x}_i^n + \Delta_{\gamma} (\delta \mathbf{x})_i^n, \quad (\delta \mathbf{x})_i^n := \mathbf{x}_i^{[\mu]} - \mathbf{x}_i^n, \\ \Delta_{\gamma} &\leq \begin{cases} -\frac{1}{2(\delta x_k)_i} \left[ (x_k)_i^n - (x_k)_{i,k,-1}^n \right], & (\delta x_k)_i < 0, \\ \frac{1}{2(\delta x_k)_i} \left[ (x_k)_{i,k,+1}^n - (x_k)_i^n \right], & (\delta x_k)_i > 0, \end{cases} \quad k = 1, 2, 3. \end{aligned}$$

Finally, the mesh velocity at  $t = t_n$  in (3.15) is determined by  $\dot{\mathbf{x}}_i^n := \Delta_{\gamma} (\delta \mathbf{x})_i^n / \Delta t_n$  with the time step size  $\Delta t_n$ , obtained by (5.1).

## 5. Numerical results

This section provides some numerical tests for the dense gas with  $\gamma = 1.0125$  to demonstrate the accuracy and effectiveness of our fifth-order accurate adaptive moving mesh ES schemes. For

convenience, the fifth-order accurate ES schemes with multi-resolution WENO on the moving mesh are denoted by “MM”, while those on the fixed uniform mesh are denoted by “UM”. In addition, our adaptive moving mesh ES schemes, using the monitor function with or without the information of fundamental derivative, are employed for the 1D and 2D cases except for the accuracy tests to illustrate the ability to capture the classical and non-classical waves. The corresponding scheme without the information of fundamental derivative in the monitor function is denoted by “MM1”. The CPU nodes of the High-performance Computing Platform of Peking University (Linux redhat environment, two Intel Xeon E5-2697A V4 per node, and core frequency of 2.6GHz) are used for the computation, and the schemes are implemented in parallel combining the MPI parts of the PLUTO code [41] with the explicit third-order SSP-RK time discretization [28]. The time step size  $\Delta t_n$  is determined by the CFL condition

$$\Delta t_n \leq \frac{\text{CFL}}{\max_i \left\{ \sum_{k=1}^d \varrho_{i,k}^n / \Delta \xi_k \right\}}, \quad (5.1)$$

where  $\varrho_{i,k}$  is the spectral radius of the eigen-matrix in the  $\xi_k$ -direction. Unless particularly stated, CFL is taken as 0.4 for the case of  $d = 1$  and  $d = 2$ , and 0.3 for  $d = 3$  in numerical experiments. The linear weights in multi-resolution WENO reconstruction are taken as  $\lambda_0 = 0.95, \lambda_1 = 0.045$  and  $\lambda_2 = 0.005$ .

**Example 5.1** (1D Smooth Sine Wave). The sine wave propagating periodically is used to test the accuracy of MM. The exact solution is given by  $(\rho, v_1, p)(x_1, t) = (0.5 + 0.2 \sin(2\pi(x_1 - t)), 1, 1)$  for  $t \geq 0$ . The domain  $\Omega_p$  is  $[0, 1]$  with periodic boundary condition and the time step size  $\Delta t_n$  is taken as  $\text{CFL} \Delta \xi_1^{5/3}$  to make the spatial error dominant. The monitor function is chosen as

$$\omega = \sqrt{1 + \frac{\alpha_1 |\nabla_{\xi} \rho|}{\max |\nabla_{\xi} \rho|} + \frac{\alpha_2 |\Delta_{\xi} \rho|}{\max |\Delta_{\xi} \rho|}}, \quad (5.2)$$

with  $\alpha_1 = 20, \alpha_2 = 15$ , and the low pass filter is used to smooth the monitor function 20 times. Figure 5.1 presents the  $\ell^1$ - and  $\ell^\infty$ -errors and the corresponding orders of convergence in  $\rho$  at  $t = 1$  by using MM with  $N_1$  cells. The results show that the MM achieves the fifth-order accuracy as expected.

**Example 5.2** (1D Riemann Problem). Several initial conditions of 1D Riemann problem are presented in Table 5.1, which have been widely used in testing the numerical schemes for the dense gas [17]. The monitor function is chosen as (4.2) with  $\delta_1 = \rho, \delta_2 = G, \alpha_1 = 1200, \alpha_2 = 3000, \kappa = 2, \alpha_3 = 5000$  for RP1 and RP2, while  $\delta_1 = \rho, \delta_2 = G, \alpha_1 = 1200, \alpha_2 = 1200, \kappa = 2, \alpha_3 = 1200$  for RP3. For a comparison, the counterparts of MM1 with  $\alpha_2 = \alpha_3 = 0$  are also implemented. The

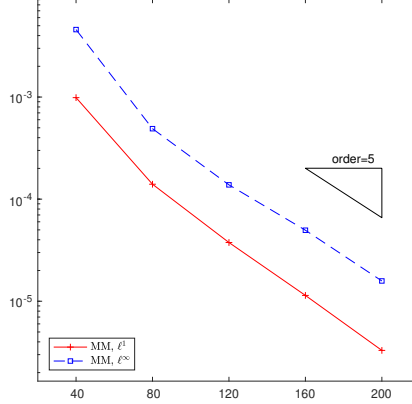


Figure 5.1: Example 5.1:  $\ell^1$ - and  $\ell^\infty$ -errors in  $\rho$  with respect to  $N_1$  at  $t = 1.0$ .

numerical results are computed by UM, MM, and MM1, and the reference solution is computed by using the second-order finite volume scheme with 10000 grid cells.

The numerical results of RP1 at  $t = 0.15Z_c^{-1/2}$  are shown in Figure 5.2. The initial fundamental derivative  $G$  is positive, as it evolves,  $G < 0$  emerges, forming a non-classical wave composed by a transonic rarefaction fan and a rarefaction shock wave. Moreover, despite the sign of  $G$  changes near  $x_1 = 0.74$ , a compressible shock satisfying the Rankine-Hugoniot jump relations is formed. The adaptive mesh points concentrate near the large gradient area of the solution as expected. MM with  $N_1 = 100$  is better than MM1 with  $N_1 = 100$  near the contact discontinuity, and superior to UM with  $N_1 = 300$  near the rarefaction shock wave, the contact discontinuity and the shock wave.

RP2 is a classical example for the dense gas with non-classical behavior. The fundamental derivative keeps negative during the flow evolution in the whole flow field. Figure 5.3 presents the numerical solution of  $\rho$ ,  $v_1$ ,  $p$  and  $G$  at  $t = 0.45Z_c^{-1/2}$ . One can see that the solution consists of a rarefaction shock wave, a contact discontinuity and a right-running compression fan. The numerical results show that MM with  $N_1 = 100$  gives sharper transitions than UM with  $N_1 = 300$  and MM1 with  $N_1 = 100$  near the rarefaction shock wave and the contact discontinuity where the mesh points concentrate.

The last example RP3 contains a  $G < 0$  region and a  $G > 0$  region during the flow evolution. In the region of the fundamental derivative changing its sign, a mixed rarefaction wave forms at  $t = 0.2Z_c^{-1/2}$  shown in Figure 5.4, while the shock wave is generated in  $G > 0$  region. Figure 5.4 shows that MM with  $N_1 = 100$  gives better results than MM1 with the same number of cells and UM with  $N_1 = 300$ , verifying the ability in capturing the localized structures of MM.

**Example 5.3** (2D Smooth Sine Wave). Similar to Example 5.1, this case is employed to evaluate the accuracy of 2D MM. The exact solutions are  $(\rho, v_1, v_2, p)(x_1, x_2, t) = (0.5 + 0.2 \sin(2\pi(x_1 + x_2 - t)), 0.5, 0.5, 1)$  for  $t \geq 0$ . The domain  $\Omega_p$  is  $[0, 1] \times [0, 1]$  divided into  $N_1 \times N_1$  cells, and periodic

|     | $\rho_l$ | $v_{1,l}$ | $p_l$ | $G_l$  | $\rho_r$ | $v_{1,r}$ | $p_r$ | $G_r$  |
|-----|----------|-----------|-------|--------|----------|-----------|-------|--------|
| RP1 | 1.818    | 0.0       | 3.000 | 4.118  | 0.275    | 0.0       | 0.575 | 0.703  |
| RP2 | 0.879    | 0.0       | 1.090 | -0.031 | 0.562    | 0.0       | 0.885 | -4.016 |
| RP3 | 0.879    | 0.0       | 1.090 | -0.031 | 0.275    | 0.0       | 0.575 | 0.703  |

Table 5.1: Example 5.2. Initial data of the Riemann problem for the one-dimensional shock tube.

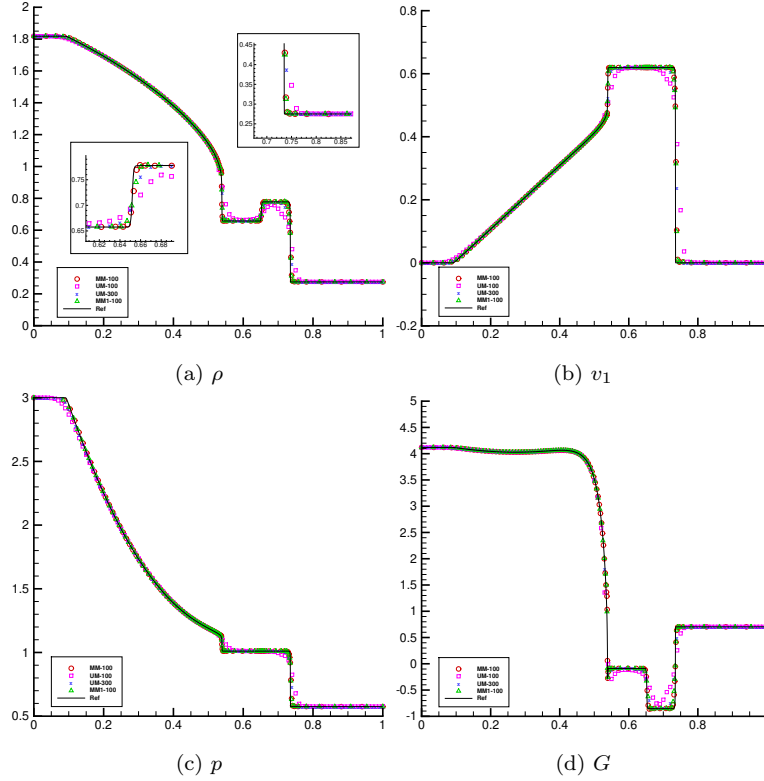


Figure 5.2: The numerical results of RP1 at  $t = 0.15Z_c^{-1/2}$ .

boundary conditions are specified on each boundary. The monitor function is chosen as Example 5.1 with  $\alpha_1 = 20, \alpha_2 = 20$ , and the number of smooth times is the same as Example 5.1. The boundary points move adaptively according to the periodic boundary conditions. Figure 5.5 shows the  $\ell^1$ - and  $\ell^\infty$ -errors and the corresponding orders of convergence in  $\rho$  at  $t = 1$  with MM, validating the fifth-order accuracy of MM.

**Example 5.4** (2D Mach Reflection). The Mach reflection is often used to test codes for the dense gas. It describes an initially shock wave propagating to the right at an angle  $\theta$  to the  $x_1$ -axis, forming complex reflection phenomena related to the angle of inclination and the shock Mach number [9]. The domain  $\Omega_p$  is  $[0, 1] \times [0, 0.5]$  and the initial conditions are given in Table 5.2. The monitor function of MM is chosen as (4.2) with  $\kappa = 1, \delta_1 = \rho, \alpha_1 = 1200, \alpha_2 = 500$ , and MM1 is the

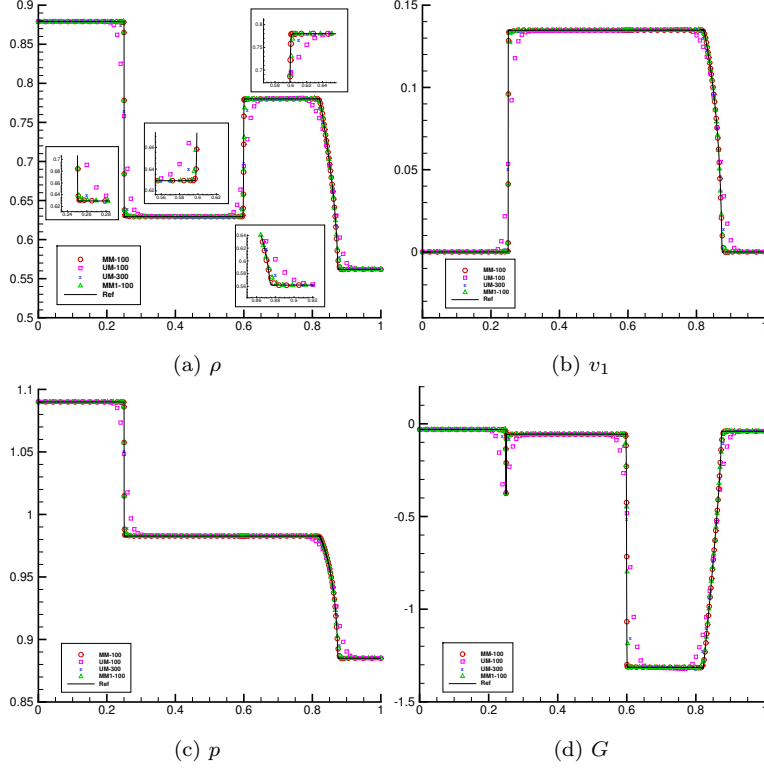


Figure 5.3: The numerical results of RP2 at  $t = 0.45Z_c^{-1/2}$ .

same as MM except for  $\alpha_2 = 0$ .

The initial data of P1 describes the van der Waals gas with small specific heat. The incidence angle of the initial shock is  $\theta = 20^\circ$ , and the Mach number is  $M_s = 1.65$ . It forms a single Mach reflection as shown in Figure 5.6. The slipstream is not very obvious due to the weak shock wave. The fundamental derivative keeps positive during the flow evolution. Figure 5.6 presents the adaptive mesh of MM with  $200 \times 100$  cells, the densities obtained respectively by MM, MM1, and UM, and the fundamental derivative given by MM at  $t = 1.0$ . It can be observed that the mesh points of the MM are adaptively concentrated near the incident shock wave, the reflected shock wave, and the Mach stem. MM with  $200 \times 100$  cells gives better results than MM1 with  $200 \times 100$  cells and UM with  $600 \times 300$  cells, when it only costs 35.5% CPU time of UM with the finer mesh shown in Table 5.3, demonstrating the efficiency of MM.

The D1 case describes an incident shock wave with  $\theta = 30^\circ$  and  $M_s = 1.05$ . Figure 5.7 gives the adaptive mesh of MM with  $200 \times 100$  cells, the densities and the fundamental derivative at  $t = 0.06$ . It is worth noting that the wave near  $x_1 = 0.52$  in Figure 5.7 is partially recompressed with the positive fundamental derivative. The solution of MM with  $200 \times 100$  cells gives sharper transitions near the shock waves than that on the uniform mesh with  $600 \times 300$  cells, since the mesh points adaptively concentrate near those regions according to the monitor function. MM with  $200 \times 100$

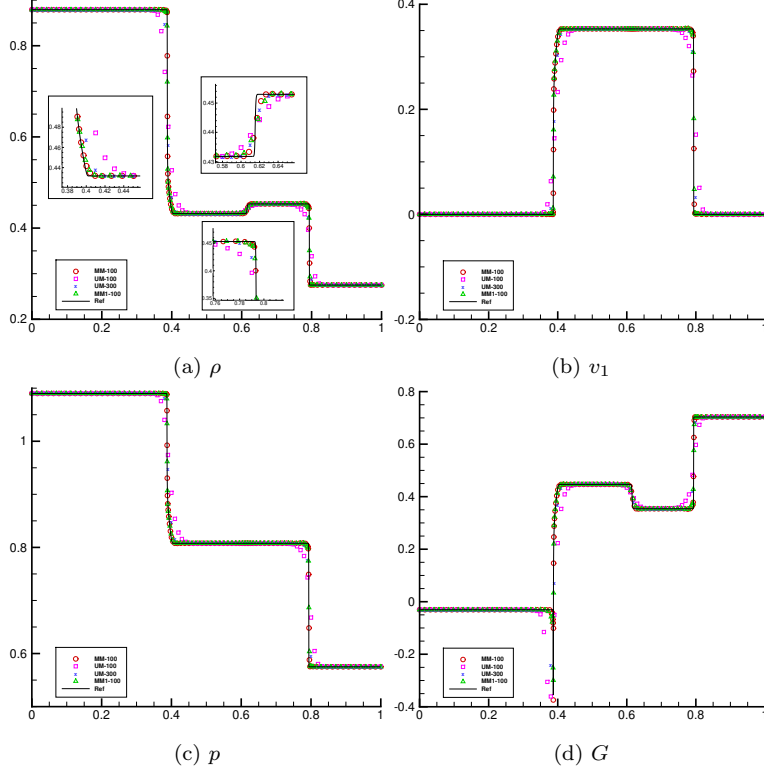


Figure 5.4: The numerical results of RP3 at  $t = 0.2Z_c^{-1/2}$ .

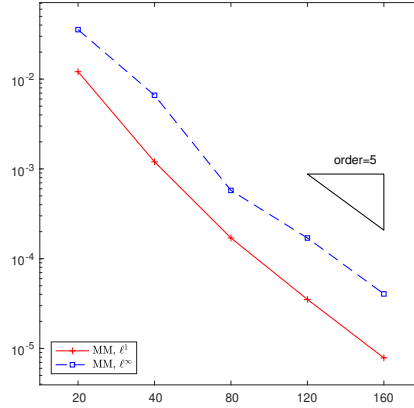


Figure 5.5: Example 5.3.  $l^1$ - and  $l^\infty$ -errors in  $\rho$  with respect to  $N_1$  at  $t = 1.0$ .

cells only take 28.6% CPU time of the uniform mesh with  $600 \times 300$  cells shown in Table 5.3, which highlight the efficiency of the adaptive moving mesh scheme.

**Example 5.5** (Backward Step Problem). This test describes a moving shock wave diffracts around a  $90^\circ$  corner given in [10]. The initial data are shown in Table 5.4. The monitor function of MM is chosen as (4.2) for TD1 and TD2 with  $\kappa = 2, \delta_1 = \rho, \delta_2 = G, \alpha_1 = 1200, \alpha_2 = 1200, \alpha_3 = 0$ , and those of MM1 are identical to MM except for  $\alpha_2 = 0$ .



|    | $\gamma$ | $\rho_l$ | $v_{1,l}$ | $v_{2,l}$ | $p_l$ | $\rho_r$ | $v_{1,r}$ | $v_{2,r}$ | $p_r$ |
|----|----------|----------|-----------|-----------|-------|----------|-----------|-----------|-------|
| P1 | 1.4      | 0.033    | 5.016     | 0.0       | 3.001 | 0.0156   | 0.0       | 0.0       | 1.0   |
| D1 | 1.0125   | 0.629    | -0.135    | 0.0       | 0.983 | 0.879    | 0.0       | 0.0       | 1.09  |

Table 5.2: Example 5.4. The initial data of the Mach reflection problem.

|     | MM ( $200 \times 100$ ) | MM1 ( $200 \times 100$ ) | UM ( $200 \times 100$ ) | UM ( $600 \times 300$ ) |
|-----|-------------------------|--------------------------|-------------------------|-------------------------|
| P1  | 3m53s                   | 3m19s                    | 37s                     | 10m57s                  |
| D1  | 4m                      | 3m37s                    | 47s                     | 13m9s                   |
| TD1 | 2m21s                   | 1m38s                    | 27s                     | 11m57s                  |
| TD2 | 3m42s                   | 2m13s                    | 21s                     | 8m8s                    |

Table 5.3: CPU times of Examples 5.4-5.5 (4 cores).

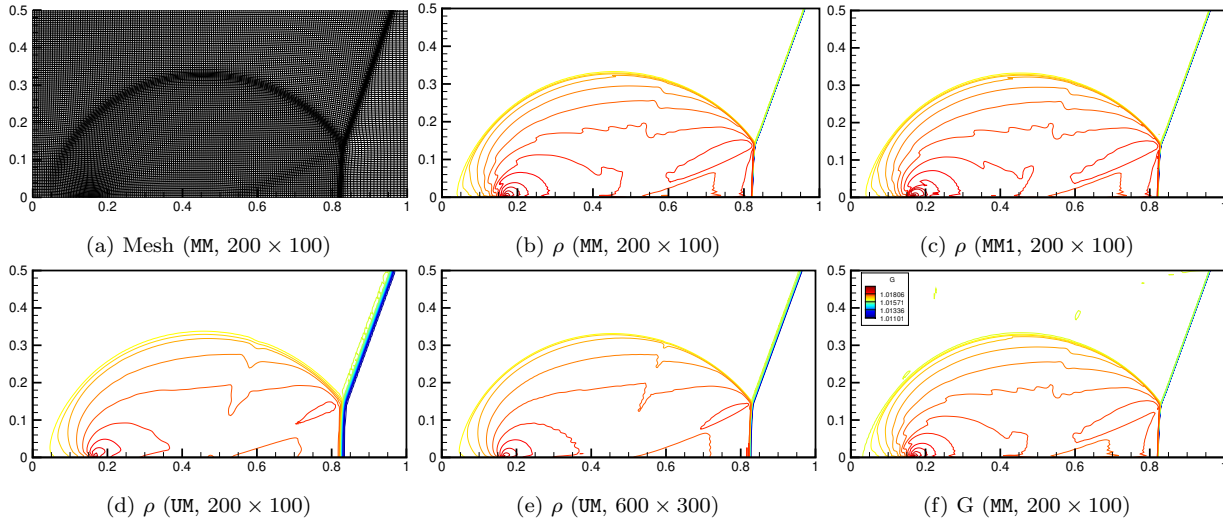


Figure 5.6: Example 5.4. Adaptive mesh of MM with  $200 \times 100$  cells, density contours (40 equally spaced contour lines) of MM, MM1 and UM, and the fundamental derivative contours (40 equally spaced contour lines) of MM at  $t = 1$ .

TD1 is about the process of a shock wave with Mach number  $M_s = 1.23$  moving to the right. The adaptive mesh of MM with  $200 \times 100$  cells and the densities at  $t = 0.55$  are shown in Figure 5.8. Figure 5.10a presents the fundamental derivative obtained by MM with  $200 \times 100$  cells. Unlike the case of ideal gas, an expansion shock wave evolves at the corner where the fundamental derivative  $G$  changes its sign. Figure 5.11a gives the densities along the line connecting  $(0.6, 0.55)$  and  $(2, 0.55)$ . One can see that the solution given by MM with  $200 \times 100$  cells is superior to the solutions given by UM with  $600 \times 300$  cells and MM1 with  $200 \times 100$  cells near  $x_1 = 1.5$ . As shown in Table 5.3, the CPU time required by the MM scheme is only 19.7% of that consumed by the UM scheme with  $600 \times 300$  cells, while MM provides a higher-resolution solution.

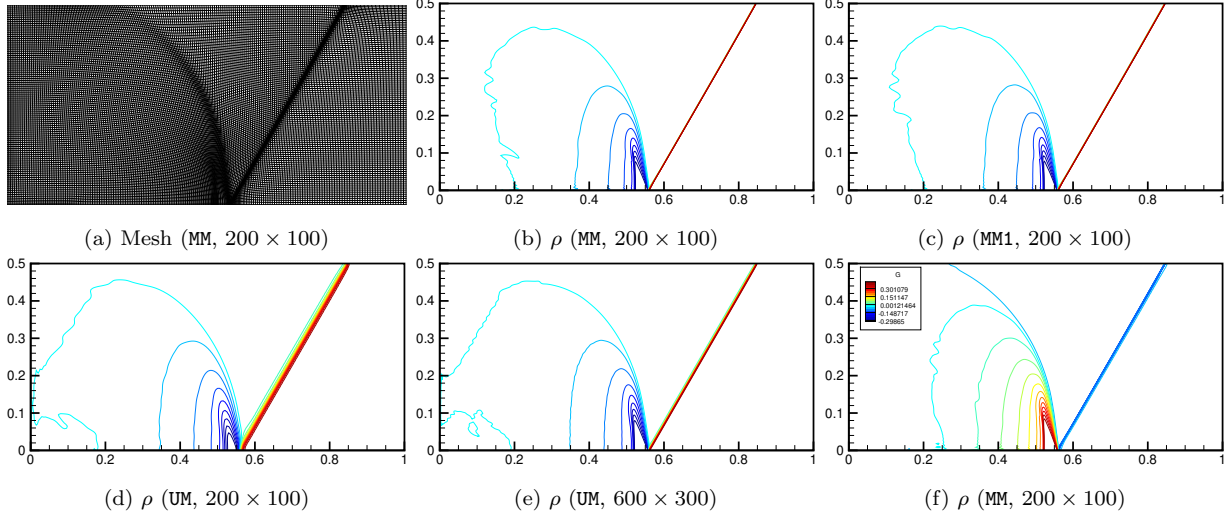


Figure 5.7: Example 5.4. Adaptive mesh of MM with  $200 \times 100$  cells, density contours (20 equally spaced contour lines) of MM, MM1 and UM, and the fundamental derivative contours (20 equally spaced contour lines) of MM at  $t = 0.06$ .

|     | $\rho_l$ | $v_{1,l}$ | $v_{2,l}$ | $p_l$ | $\rho_r$ | $v_{1,r}$ | $v_{2,r}$ | $p_r$ |
|-----|----------|-----------|-----------|-------|----------|-----------|-----------|-------|
| TD1 | 0.85     | 0.64      | 0.0       | 1.01  | 0.28     | 0.0       | 0.0       | 0.58  |
| TD2 | 0.62     | -0.14     | 0.0       | 0.98  | 0.88     | 0.0       | 0.0       | 1.09  |

Table 5.4: Example 5.5. The initial data of flow over a backward step.

TD2 describes a shock wave with  $M_s = 1.05$  that spreads into a fan near the corner during flow evolution. Figure 5.9 gives the adaptive mesh of MM with  $200 \times 100$  cells and the densities at  $t = 1.5$ . One can see that the mesh points adaptively concentrate near the large gradient area of the density and fundamental derivative. The  $G > 0$  region only appears near the step at  $x = 0.95$  shown in 5.10b. Figure 5.11b depicts the densities along the line connecting  $(0.6, 0.55)$  and  $(2, 0.55)$ . It is evident that MM captures the localized structures better than MM1 near  $x_1 = 0.95$  with the same number of cells. Table 5.3 tells us that MM is efficient since it costs 45.5% CPU time of UM with a finer mesh, but gets better results.

**Example 5.6** (3D Smooth Sin Wave). Similar to Example 5.1, this example is to check the accuracy of 3D MM via the 3D sin wave moving periodically with a constant velocity in the domain  $\Omega_p = [0, 1]^3$ . The exact solutions are given by

$$(\rho, v_1, v_2, v_3, p) = (0.5 + 0.2 \sin(2\pi(x_1 + x_2 + x_3 - 0.9t)), 0.3, 0.3, 0.3, 1).$$

The monitor function and the number of smooth times are the same as Example 5.1. The boundary points move according to the periodic boundary conditions. The linear weights in multi-resolution WENO reconstruction are taken as  $\lambda_0 = \lambda_1 = \lambda_2 = 1/3$  in this test. Figure 5.12 presents the  $\ell^1$ -

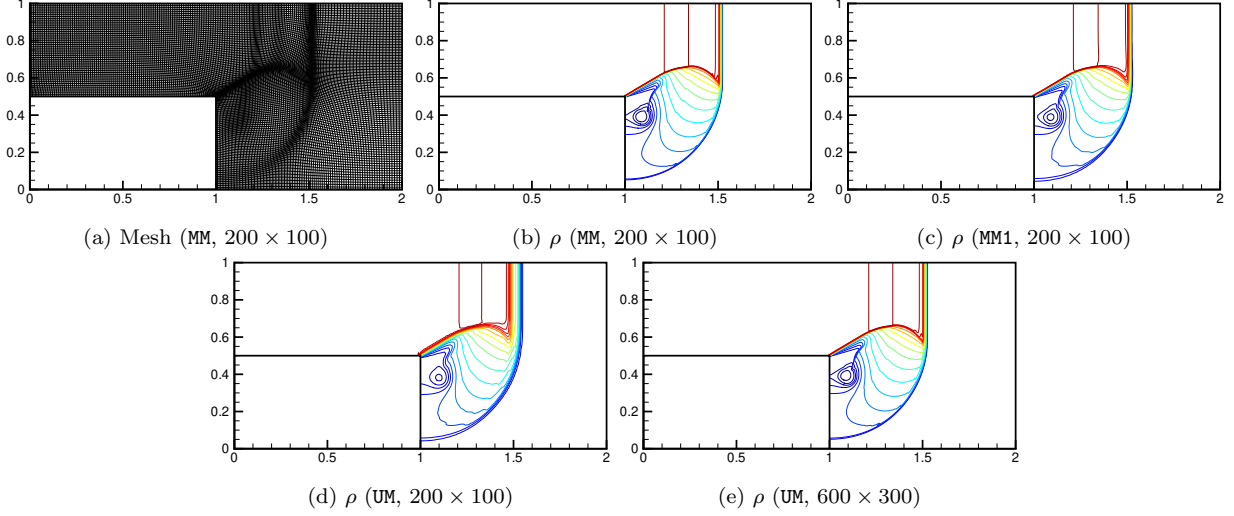


Figure 5.8: Example 5.5. Adaptive mesh of  $\text{MM}$  with  $200 \times 100$  cells, density contours (20 equally spaced contour lines) of  $\text{MM}$ ,  $\text{MM1}$  and  $\text{UM}$  at  $t = 0.55$ .

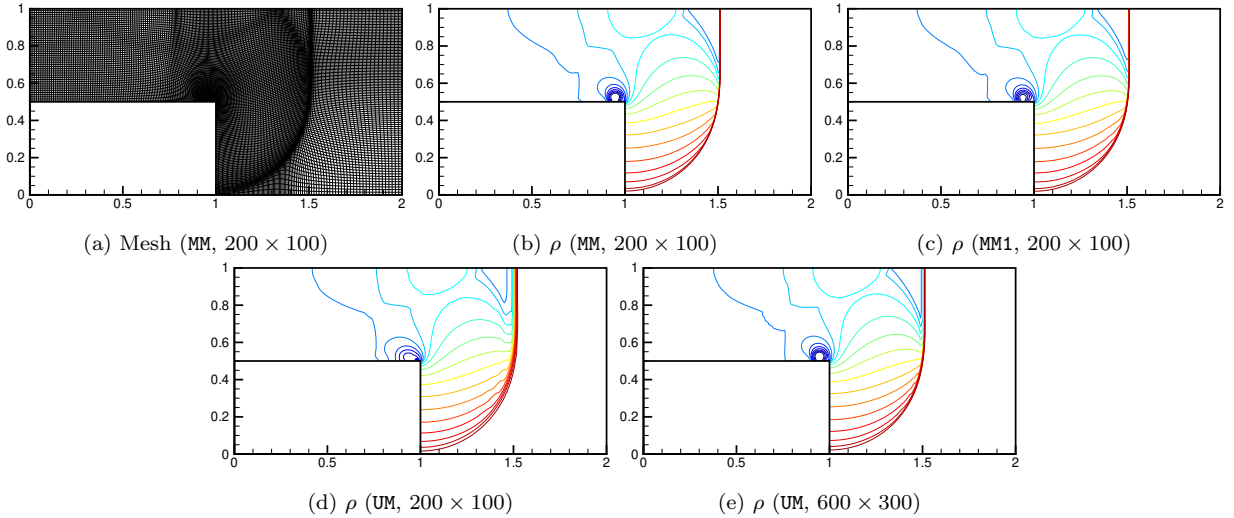


Figure 5.9: Example 5.5. Adaptive mesh of  $\text{MM}$  with  $200 \times 100$  cells, density contours (20 equally spaced contour lines) of  $\text{MM}$ ,  $\text{MM1}$  and  $\text{UM}$  at  $t = 1.5$ .

and  $\ell^\infty$ -errors and the corresponding orders of convergence in  $\rho$  at  $t = 0.1$  with  $\text{MM}$ , which shows that  $\text{MM}$  can achieve the fifth-order accuracy as expected.

**Example 5.7 (3D Spherical Symmetric Shock Tube).** This is an extension of 1D Riemann problem. The initial data are

$$(\rho, v_1, v_2, v_3, p) = \begin{cases} (1.818, 0, 0, 0, 3.0), & \sqrt{x_1^2 + x_2^2 + x_3^2} < 0.5, \\ (0.275, 0, 0, 0, 0.575), & \text{otherwise.} \end{cases}$$

The domain  $\Omega_p$  is  $[0, 1]^3$ , and the monitor function of  $\text{MM}$  is the same as Example 5.5. The numerical

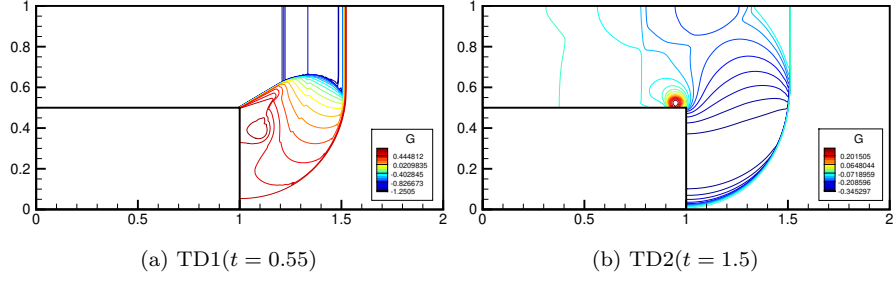


Figure 5.10: Example 5.5. The fundamental derivative contours (20 equally spaced contour lines) obtained by MM with  $200 \times 100$  cells for TD1 (left) and TD2 (right).

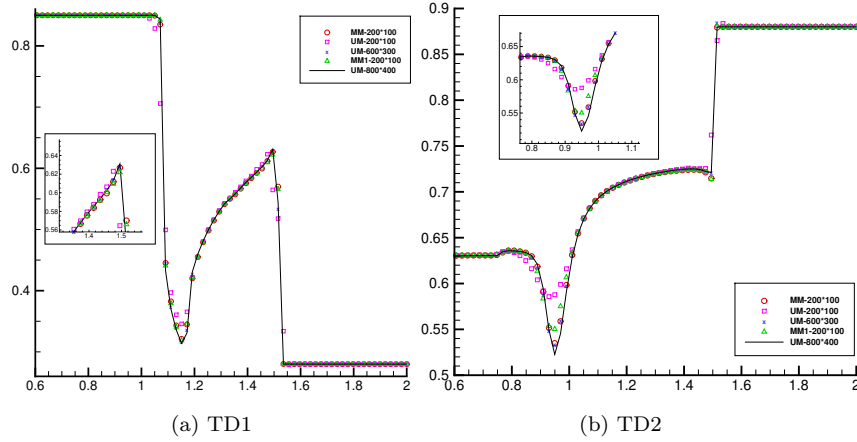


Figure 5.11: Example 5.5. Density  $\rho$  along the line connecting  $(0.6, 0.55)$  and  $(2, 0.55)$  for TD1 (left) and TD2 (right), respectively.

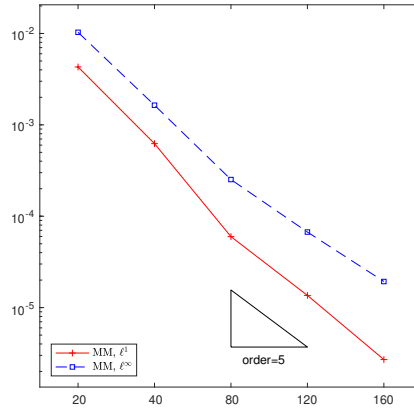


Figure 5.12: Example 5.6.  $\ell^1$ - and  $\ell^\infty$ -errors and orders of convergence in  $\rho$  with respect to  $N_1$  at  $t = 0.1$ .

results of  $\rho$  along the volume diagonal connecting  $(0, 0, 0)$  and  $(1, 1, 1)$  are shown in 5.13b with the reference solution obtained by a second-order finite volume scheme using 10000 cells in 1D spherical coordinates. The adaptive mesh points gather near the large gradient area of the density and the fundamental derivative as shown in Figure 5.13a. MM with  $100^3$  mesh cells is better than UM with

$100^3$  mesh cells near the shock and the rarefaction shock, comparable with UM with  $200^3$  mesh cells. It indicates the flow characteristics can be precisely captured by MM. From Table 5.5, the CPU time of MM with  $100^3$  cells is 12% of UM with  $200^3$  cells, verifying the efficiency of MM.

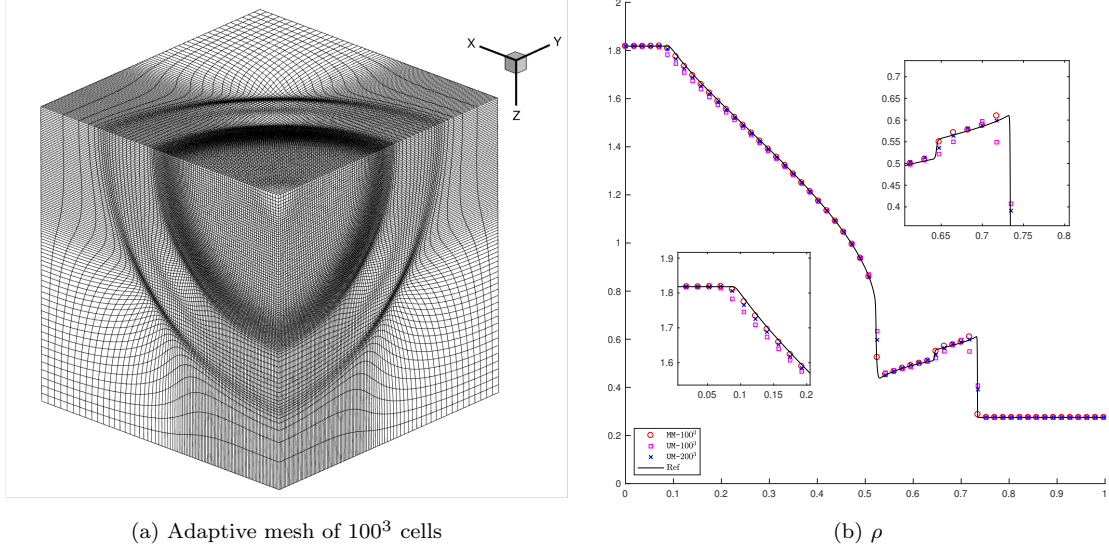


Figure 5.13: Example 5.7. Adaptive mesh of MM and  $\rho$  along the line connecting  $(0, 0, 0)$  and  $(1, 1, 1)$  at  $t = 0.2$ .

**Example 5.8** (3D Jet Injection). This test considers a simplified form of fuel injection on the domain  $\Omega_p = [0, 7.5] \times [-2.5, 2.5] \times [-2.5, 2.5]$ . Here, a higher-density fluid is injected on the subdomain  $[0, 0.6] \times [-0.3, 0.3] \times [-0.3, 0.3]$ , the initial data are

$$(\rho, v_1, v_2, v_3, p) = (2, 1, 0, 0, 10).$$

The rest of domain  $\Omega_p$  is filled with a stationary lower-density fluid with

$$(\rho, v_1, v_2, v_3, p) = (0.5, 0, 0, 0, 10).$$

The monitor function is chosen as (4.2), with  $\kappa = 2, \sigma_1 = \rho, \sigma_2 = G, \alpha_1 = \alpha_2 = 1200, \alpha_3 = 0$ . Figure 5.14 gives the close-up of the adaptive mesh, three offset 2D slices, the iso-surfaces of  $\rho = 0.88$ , and two surface meshes at  $t = 4$ . Figure 5.15 compares the schlieren images on the slice  $x_3 = 0$  given by  $\Phi = \exp(-5|\nabla\rho|/|\nabla\rho|_{\max})$ , where the top parts are the results obtained by MM with  $150 \times 100 \times 100$  cells, while the left and right bottom half parts are those obtained by UM with  $150 \times 100 \times 100$  cells and  $300 \times 200 \times 200$  cells, respectively. It can be seen that MM is efficient since the CPU time of MM with  $150 \times 100 \times 100$  cells is 34.9% of UM with  $300 \times 200 \times 200$  cells shown in Table 5.5, and the solution obtained by MM is superior to that obtained by UM with  $300 \times 200 \times 200$  cells.



|             | MM                                    | UM                                    | UM                                    |
|-------------|---------------------------------------|---------------------------------------|---------------------------------------|
| Example 5.7 | 9m45s ( $100^3$ )                     | 3m45s ( $100^3$ )                     | 1h21m ( $200^3$ )                     |
| Example 5.8 | 4h32m ( $150 \times 100 \times 100$ ) | 49m2s ( $150 \times 100 \times 100$ ) | 13h0m ( $300 \times 200 \times 200$ ) |

Table 5.5: CPU times of Examples 5.7-5.8 (32 cores).

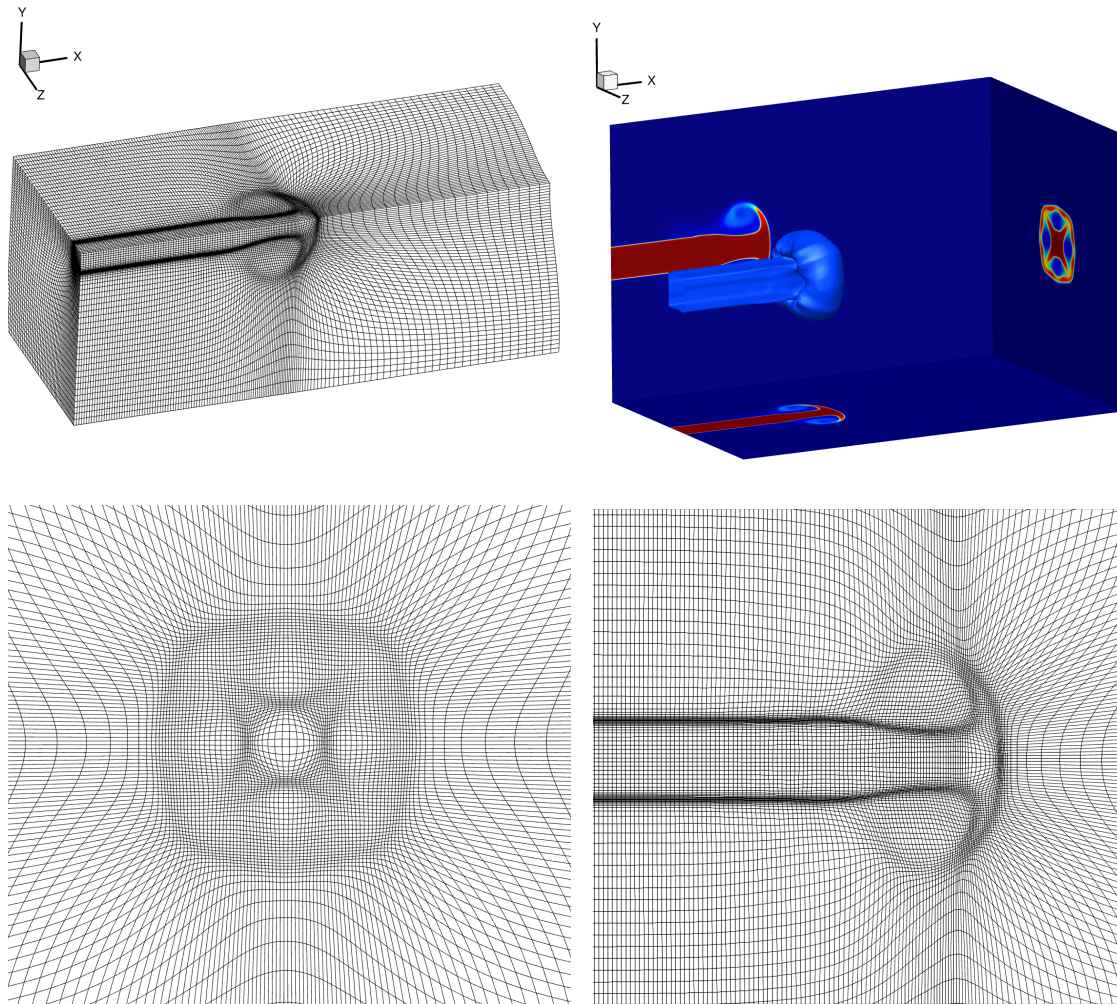


Figure 5.14: Example 5.8. Adaptive meshes and  $\rho$  at  $t = 4$ . Top left: close-up of the adaptive mesh,  $i_1 \in [1, 140]$ ,  $i_2 \in [1, 50]$ ,  $i_3 \in [1, 50]$ ; top right: the iso-surface of  $\rho = 0.88$ ; bottom left: the surface mesh with  $i_1 = 95$ ; bottom right: the surface mesh with  $i_3 = 50$ .

## 6. Conclusion

This paper developed the high-order entropy stable (ES) finite difference schemes for multi-dimensional compressible Euler equations with the van der Waals equation of state (EOS) on adaptive moving meshes. Similar to the schemes proposed in [23], the two-point symmetric EC flux was first technically constructed with the thermodynamic entropy and suitably chosen parameter

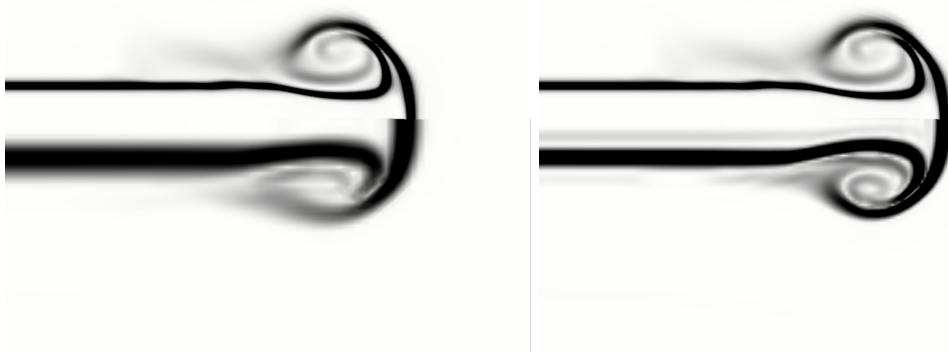


Figure 5.15: Example 5.8. Schlieren images on the slice  $x_3 = 0$  at  $t = 4$ . Left: **MM** (top half) and **UM** (bottom half) with  $150 \times 100 \times 100$ ; right: **MM** with  $150 \times 100 \times 100$  (top half) and **UM** with  $300 \times 200 \times 200$  (bottom half).

vectors. It is worth reminding that the nonlinearity arising from the van der Waals EOS brings challenges for the derivation of such EC fluxes. The high-order EC fluxes in curvilinear coordinates were derived by using the high-order discrete GCLs and the linear combination of the two-point EC fluxes. To suppress the oscillation near the shock waves, the high-order dissipation terms based on the newly derived complex scaled eigenmatrix and multi-resolution WENO reconstruction were added to the EC schemes to derive the high-order semi-discrete ES schemes which satisfied the semi-discrete entropy inequality. The explicit third-order SSP-RK time discretization and the adaptive moving mesh scheme were implemented to construct the fully-discrete ES adaptive moving mesh finite difference schemes. Several 1D, 2D and 3D numerical tests were used to verify the accuracy, effectiveness, and ability to capture the classical and non-classical waves of the proposed schemes on the parallel computer system with the MPI programming.

## Appendix A. Different forms of linear equations to obtain two-points EC flux

This appendix presents the main results on three different forms of linear equations obtained with three different parameter vectors to construct the explicit expression of two-points symmetric EC flux for the 1D compressible Euler equations.

If choosing the parameter vector

$$\mathbf{z} = (z_1, z_2, z_3)^T = \left( \frac{3-\rho}{T}, \frac{T}{(3-\rho)^2}, v_1 \right)^T,$$

and the identities

$$\llbracket -s \rrbracket = \frac{1}{\delta \llbracket z_1^2 z_2 \rrbracket \ln} \llbracket \frac{1}{T} \rrbracket + \frac{3 \llbracket z_1 z_2 \rrbracket}{\llbracket 3 z_1 z_2 - 1 \rrbracket \ln},$$

$$\begin{aligned}
\left[\left[\frac{1}{T}\right]\right] &= \left[\left(z_1 z_2^{\frac{1}{2}}\right)^2\right] = 2\{\{z_1 z_2^{\frac{1}{2}}\}\} \left( \frac{\{\{z_1\}\}}{2\{\{z_2^{\frac{1}{2}}\}\}} \llbracket z_2 \rrbracket + \{\{z_2^{\frac{1}{2}}\}\} \llbracket z_1 \rrbracket \right) \\
&= \{\{z_1^2\}\} \llbracket z_2 \rrbracket + 2\{\{z_1\}\} \{\{z_2\}\} \llbracket z_1 \rrbracket \\
&= \{\{z_1\}\} \{\{z_2\}\} \llbracket z_1 \rrbracket + \{\{z_1 z_2\}\} \llbracket z_1 \rrbracket + \{\{z_1\}\}^2 \llbracket z_2 \rrbracket \\
&=: A \llbracket z_1 \rrbracket + B \llbracket z_2 \rrbracket,
\end{aligned}$$

then the jump of  $\mathbf{V}$  can be expressed as

$$\left\{ \begin{aligned}
\llbracket \mathbf{V}_1 \rrbracket &= \left( \frac{1}{\delta \{\{1/T\}\}^{\ln}} A + \frac{3\{\{z_2\}\}}{\{\{3z_1 z_2 - 1\}\}^{\ln}} + 3\{\{z_2\}\} - \frac{27}{4} A - \frac{\{\{z_3^2\}\}}{2} A + \frac{9}{4} \right) \llbracket z_1 \rrbracket \\
&\quad + \left( \frac{1}{\delta \{\{1/T\}\}^{\ln}} B + \frac{3\{\{z_1\}\}}{\{\{3z_1 z_2 - 1\}\}^{\ln}} + 3\{\{z_1\}\} - \frac{27}{4} B - \frac{\{\{z_3^2\}\}}{2} B \right) \llbracket z_2 \rrbracket - \{\{1/T\}\} \{\{z_3\}\} \llbracket z_3 \rrbracket, \\
\llbracket \mathbf{V}_2 \rrbracket &= \{\{z_3\}\} A \llbracket z_1 \rrbracket + \{\{z_3\}\} B \llbracket z_2 \rrbracket + \{\{1/T\}\} \llbracket z_3 \rrbracket, \\
\llbracket \mathbf{V}_3 \rrbracket &= -A \llbracket z_1 \rrbracket - B \llbracket z_2 \rrbracket.
\end{aligned} \right.$$

The coefficient matrix of the above system of linear equations is given as

$$\begin{bmatrix}
\frac{1}{\delta \{\{1/T\}\}^{\ln}} A + \frac{3\{\{z_2\}\}}{\{\{3z_1 z_2 - 1\}\}^{\ln}} + 3\{\{z_2\}\} - \frac{27}{4} A - \frac{\{\{z_3^2\}\}}{2} A + \frac{9}{4} & \{\{z_3\}\} A & -A \\
\frac{1}{\delta \{\{1/T\}\}^{\ln}} B + \frac{3\{\{z_1\}\}}{\{\{3z_1 z_2 - 1\}\}^{\ln}} + 3\{\{z_1\}\} - \frac{27}{4} B - \frac{\{\{z_3^2\}\}}{2} B & \{\{z_3\}\} B & -B \\
-\{\{1/T\}\} \{\{z_3\}\} & \{\{1/T\}\} & 0
\end{bmatrix}^T,$$

whose determinant is

$$\begin{aligned}
&\{\{3/T\}\} \left( \frac{B \{\{z_2\}\} - A \{\{z_1\}\}}{\{\{3z_1 z_2 - 1\}\}^{\ln}} + B \{\{z_2\}\} - A \{\{z_1\}\} + \frac{3}{4} \right) \\
&= \{\{3/T\}\} \left( \frac{-\{\{z_1 z_2\}\} \{\{z_1\}\}}{\{\{3z_1 z_2 - 1\}\}^{\ln}} - \{\{z_1 z_2\}\} \{\{z_1\}\} + \frac{3}{4} \right).
\end{aligned}$$

It is not difficult to find that even in the case of  $T_l = T_r = \{\{T\}\} > 1$ , there exist admissible states  $\rho_l, \rho_r$  such that the determinant is zero.

If choosing the following parameter vector

$$\mathbf{z} = (z_1, z_2, z_3)^T = \left(\rho, \frac{1}{T}, v_1\right)^T,$$

then the jump of  $\mathbf{V}$  can be similarly expressed as

$$\left\{ \begin{aligned}
\llbracket \mathbf{V}_1 \rrbracket &= \left( \frac{1}{\{\{z_1\}\}^{\ln}} + \frac{1}{\{\{3 - z_1\}\}^{\ln}} + \frac{3}{(3 - z_{1,l})(3 - z_{1,r})} - \frac{9}{4} \{\{z_2\}\} \right) \llbracket z_1 \rrbracket \\
&\quad + \left( \frac{1}{\delta \{\{z_2\}\}^{\ln}} - \frac{9}{4} \{\{z_1\}\} - \frac{\{\{z_3^2\}\}}{2} \right) \llbracket z_2 \rrbracket - \{\{z_2\}\} \{\{z_3\}\} \llbracket z_3 \rrbracket, \\
\llbracket \mathbf{V}_2 \rrbracket &= \{\{z_3\}\} \llbracket z_2 \rrbracket + \{\{z_2\}\} \llbracket z_3 \rrbracket, \\
\llbracket \mathbf{V}_3 \rrbracket &= -\llbracket z_2 \rrbracket.
\end{aligned} \right.$$



The coefficient matrix of the above system of linear equations is given by

$$\begin{bmatrix} \frac{1}{\{\{z_1\}\}^{\ln}} + \frac{1}{\{\{3-z_1\}\}^{\ln}} + \frac{3}{(3-z_{1,l})(3-z_{1,r})} - \frac{9}{4}\{\{z_2\}\} & 0 & 0 \\ \frac{1}{\delta\{\{z_2\}\}^{\ln}} - \frac{9}{4}\{\{z_1\}\} - \frac{\{\{z_3^2\}\}}{2} & \{\{z_3\}\} & -1 \\ -\{\{z_2\}\}\{\{z_3\}\} & \{\{z_2\}\} & 0 \end{bmatrix}^T,$$

and the corresponding determinant is

$$\{\{z_2\}\} \left( \frac{1}{\{\{z_1\}\}^{\ln}} + \frac{1}{\{\{3-z_1\}\}^{\ln}} + \frac{3}{(3-z_{1,l})(3-z_{1,r})} - \frac{9}{4}\{\{z_2\}\} \right),$$

which is smaller than the determinant obtained using the parameter vector (3.6).

If choosing the following parameter vector

$$\mathbf{z} = (z_1, z_2, z_3)^T = \left( -\frac{9}{8T} + \frac{1}{3-\rho}, \frac{1}{3-\rho}, v_1 \right)^T,$$

and the identity  $\{\{1/T\}\} = \frac{8}{9}\{\{z_2\}\} - \frac{8}{9}\{\{z_1\}\} =: A\{\{z_1\}\} + B\{\{z_2\}\}$ , then the jump of  $\mathbf{V}$  can be expressed as

$$\begin{cases} \mathbf{V}_1 = \left( \frac{1}{\delta\{\{1/T\}\}^{\ln}} A + 6 - \{\{2/z_2\}\} - \frac{\{\{z_3^2\}\}}{2} A \right) \{\{z_1\}\} \\ \quad + \left( \frac{1}{\delta\{\{1/T\}\}^{\ln}} B - 3 + \frac{3}{\{\{3-\rho\}\}^{\ln}} + \frac{\{\{z_1\}\}}{\{\{z_2\}\}} \{\{2/z_2\}\} - \frac{\{\{z_3^2\}\}}{2} B \right) \{\{z_2\}\} - \{\{1/T\}\} \{\{z_3\}\} \{\{z_3\}\}, \\ \mathbf{V}_2 = \{\{z_3\}\} A \{\{z_1\}\} + \{\{z_3\}\} B \{\{z_2\}\} + \{\{1/T\}\} \{\{z_3\}\}, \\ \mathbf{V}_3 = -A \{\{z_1\}\} - B \{\{z_2\}\}. \end{cases}$$

The coefficient matrix of the above system of linear equations is given by

$$\begin{bmatrix} \frac{1}{\delta\{\{1/T\}\}^{\ln}} A + 6 - \{\{2/z_2\}\} - \frac{\{\{z_3^2\}\}}{2} A & \{\{z_3\}\} A & -A \\ \frac{1}{\delta\{\{1/T\}\}^{\ln}} B - 3 + \frac{3}{\{\{3-\rho\}\}^{\ln}} - \frac{\{\{z_3^2\}\}}{2} B + \frac{\{\{z_1\}\}}{\{\{z_2\}\}} \{\{2/z_2\}\} & \{\{z_3\}\} B & -B \\ -\{\{1/T\}\} \{\{z_3\}\} & \{\{1/T\}\} & 0 \end{bmatrix}^T,$$

whose determinant is

$$\begin{aligned} & \{\{1/T\}\} \left( 6B + 3A - B \{\{2/z_2\}\} - \frac{3A}{\{\{3-\rho\}\}^{\ln}} - \frac{\{\{z_1\}\}}{\{\{z_2\}\}} \{\{2/z_2\}\} A \right) \\ & = \frac{8}{9} \{\{1/T\}\} \left[ 3 - \{\{2/z_2\}\} + \frac{3}{\{\{3-\rho\}\}^{\ln}} + \frac{\{\{z_1\}\}}{\{\{z_2\}\}} \{\{2/z_2\}\} \right]. \end{aligned}$$

It is worth noting that the existence and uniqueness of solutions for the systems of linear equations are crucial for obtaining an explicit form of the two-point EC fluxes. The above three linear systems may not obtain the well-defined explicit expressions of the two-point EC fluxes, due to the possibility of their determinant being zero. So the construction of two-point EC fluxes is nontrivial, especially for the van der Waals gas under consideration.

## Acknowledgment

The work was partially supported by the National Key R&D Program of China (Project Numbers 2020YFA0712000 & 2020YFE0204200) and the National Natural Science Foundation of China (Nos. 12171227, 12288101, & 12326314).

## References

- [1] R. Abgrall, An extension of Roe's upwind scheme to algebraic equilibrium real gas models, *Comput. & Fluids*, 19 (1991), 171-182.
- [2] J. Anders, W. Anderson, and A. Murthy, Transonic similarity theory applied to a supercritical airfoil in heavy gas, *J. Aircr.*, 36 (1999), 957-964.
- [3] B.M. Argrow, Computational analysis of dense gas shock tube flow, *Shock Waves*, 6 (1996), 241-248.
- [4] H.A. Bethe, On the theory of shock waves for an arbitrary equation of state, In: *Classic Papers in Shock Compression Science*, Johnson, J.N., Chéret, R. (eds), Springer New York, 1998, 421-495.
- [5] D. Bhoriya and H. Kumar, Entropy-stable schemes for relativistic hydrodynamics equations, *Z. Angew. Math. Phys.*, 71 (2020), 1-29.
- [6] B. Biswas and R.K. Dubey, Low dissipative entropy stable schemes using third order WENO and TVD reconstructions, *Adv. Comput. Math.*, 44 (2018), 1153-1181.
- [7] J.U. Brackbill, An adaptive grid with directional control, *J. Comput. Phys.*, 108 (1993), 38-50.
- [8] J.U. Brackbill and J.S. Saltzman, Adaptive zoning for singular problems in two dimensions, *J. Comput. Phys.*, 46 (1982), 342-368.
- [9] B.P. Brown and B.M. Argrow, Two-dimensional shock tube flow for dense gases, *J. Fluid Mech.*, 349 (1997), 95-115.
- [10] B.P. Brown and B.M. Argrow, Nonclassical dense gas flows for simple geometries, *AIAA J.*, 36 (1998), 1842-1847.
- [11] C.J. Budd, W.Z. Huang, and R.D. Russell, Adaptivity with moving grids, *Acta Numer.*, 18 (2009), 111-241.

- [12] W. Cao, W. Huang, and R.D. Russell, An  $r$ -adaptive finite element method based upon moving mesh PDEs, *J. Comput. Phys.*, 149 (1999), 221-244.
- [13] M.H. Carpenter, T.C. Fisher, E.J. Nielsen, and S.H. Frankel, Entropy stable spectral collocation schemes for the Navier-Stokes equations: Discontinuous interfaces, *SIAM J. Sci. Comput.*, 36 (2014), B835-B867.
- [14] H.D. Ceniceros and T.Y. Hou, An efficient dynamically adaptive mesh for potentially singular solutions, *J. Comput. Phys.*, 172 (2001), 609-639.
- [15] P. Chandrashekar, Kinetic energy preserving and entropy stable finite volume schemes for compressible Euler and Navier-Stokes equations, *Commun. Comput. Phys.*, 14 (2013), 1252-1286.
- [16] T.H. Chen and C.W. Shu, Review of entropy stable discontinuous Galerkin methods for systems of conservation laws on unstructured simplex meshes, *CSIAM Trans. Appl. Math.*, 1 (2020), 1-52.
- [17] P. Cinnella, Roe-type schemes for dense gas flow computations, *Comput. & Fluids*, 35 (2006), 1264-1281.
- [18] P. Colonna, A. Guardone, and N.R. Nannan, Siloxanes: A new class of candidate Bethe-Zel'dovich-Thompson fluids, *Phys. Fluids*, 19 (2007), 086102.
- [19] M.S. Cramer, Structure of weak shocks in fluids having embedded regions of negative nonlinearity, *Phys. Fluids*, 30 (1987), 3034-3044.
- [20] M.S. Cramer and L.M. Best, Steady, isentropic flows of dense gases, *Phys. Fluids*, 3 (1991), 219-226.
- [21] M.G. Crandall and A. Majda, Monotone difference approximations for scalar conservation laws, *Math. Comp.*, 34 (1980), 1-21.
- [22] J.M. Duan and H.Z. Tang, Entropy stable adaptive moving mesh schemes for 2D and 3D special relativistic hydrodynamics, *J. Comput. Phys.*, 426(2021), 109949.
- [23] J.M. Duan and H.Z. Tang, High-order accurate entropy stable adaptive moving mesh finite difference schemes for special relativistic (magneto)hydrodynamics, *J. Comput. Phys.*, 456 (2022), 111038.

- [24] U.S. Fjordholm, S. Mishra, and E. Tadmor, Well-balanced and energy stable schemes for the shallow water equations with discontinuous topography, *J. Comput. Phys.*, 230 (2011), 5587-5609.
- [25] U.S. Fjordholm, S. Mishra, and E. Tadmor, Arbitrarily high-order accurate entropy stable essentially non-oscillatory schemes for systems of conservation laws, *SIAM J. Numer. Anal.*, 50 (2012), 544-573.
- [26] G.J. Gassner, A skew-symmetric discontinuous Galerkin spectral element discretization and its relation to SBP-SAT finite difference methods, *SIAM J. Sci. Comput.*, 35 (2013), 1233-1253.
- [27] P. Glaister, An approximate linearised Riemann solver for the Euler equations for real gases, *J. Comput. Phys.*, 74 (1988), 382-408.
- [28] S. Gottlieb, C.W. Shu, and E. Tadmor, Strong stability-preserving high-order time discretization methods, *SIAM Review*, 43 (2001), 89-112.
- [29] A. Guardone and L. Quartapelle, *Exact Roe linearization for van der Waals' gas*, Springer US, New York, NY (2001), 419-424.
- [30] A. Guardone and L. Vigevano, Roe linearization for the van der Waals gas, *J. Comput. Phys.*, 175 (2002), 50-78.
- [31] A. Harten, J.M. Hyman, and P.D. Lax, On finite-difference approximations and entropy conditions for shocks, *Comm. Pure Appl. Math.*, 29 (1976), 297-322.
- [32] P. He and H.Z. Tang, An adaptive moving mesh method for two-dimensional relativistic hydrodynamics, *Commun. Comput. Phys.*, 11 (2012), 114-146.
- [33] P. He and H.Z. Tang, An adaptive moving mesh method for two-dimensional relativistic magnetohydrodynamics, *Comput. & Fluids*, 60 (2012), 1-20.
- [34] A. Hildebrand and S. Mishra, Entropy stable shock capturing space-time discontinuous Galerkin schemes for systems of conservation laws, *Numer. Math.*, 126 (2014), 103-151.
- [35] F. Ismail and P.L. Roe, Affordable, entropy-consistent Euler flux functions II: Entropy production at shocks, *J. Comput. Phys.*, 228 (2009), 5410-5436.
- [36] K.C. Lambrakis and P.A. Thompson, Existence of real fluids with a negative fundamental derivative  $\Gamma$ , *Phys. Fluids*, 15 (1972), 933-935.

- [37] P.G. LeFloch, J.M. Mercier, and C. Rohde, Fully discrete entropy conservative schemes of arbitrary order, *SIAM J. Numer. Anal.*, 40 (2002), 1968-1992.
- [38] R. Li, T. Tao, and P.W. Zhang, Moving mesh methods in multiple dimensions based on harmonic maps, *J. Comput. Phys.*, 170 (2001), 562-588.
- [39] S. Li and L. Petzold, Moving mesh methods with upwinding schemes for time-dependent PDEs, *J. Comput. Phys.*, 131 (1997), 368-377.
- [40] S.T. Li, J.M. Duan, and H.Z. Tang, High-order accurate entropy stable adaptive moving mesh finite difference schemes for (multi-component) compressible euler equations with the stiffened equation of state, *Comput. Methods Appl. Mech. Engrg.*, 399 (2022), 115311.
- [41] A. Mignone, G. Bodo, S. Massaglia, T. Matsakos, O. Tesileanu, C. Zanni, and A. Ferrari, PLUTO: A numerical code for computational astrophysics, *Astrophys. J. Suppl. Ser.*, 170 (2007), 228-242.
- [42] S. Osher, Riemann solvers, the entropy condition, and difference approximations, *SIAM J. Numer. Anal.*, 21 (1984), 217-235.
- [43] S. Osher and E. Tadmor, On the convergence of difference approximations to scalar conservation laws, *Math. Comp.*, 50 (1988), 19-51.
- [44] E.M. Prodanov, Mathematical analysis of the van der Waals equation, *Phys. B: Condens. Matter*, 640 (2022), 414077.
- [45] W.Q. Ren and X.P. Wang, An iterative grid redistribution method for singular problems in multiple dimensions, *J. Comput. Phys.*, 159 (2000), 246-273.
- [46] G.H. Schnerr and P. Leidner, Diabatic supersonic flows of dense gases, *Phys. Fluids*, 3 (1991), 2445-2458.
- [47] K.M. Shyue, A fluid-mixture type algorithm for compressible multicomponent flow with van der Waals equation of state, *J. Comput. Phys.*, 156 (1999), 43-88.
- [48] J.M. Stockie, J.A. Mackenzie, and R.D. Russell, A moving mesh method for one-dimensional hyperbolic conservation laws, *SIAM J. Sci. Comput.*, 22 (2001), 1791-1813.
- [49] E. Tadmor, The numerical viscosity of entropy stable schemes for systems of conservation laws, I, *Math. Comp.*, 49 (1987), 91-103.

- [50] E. Tadmor, Entropy stability theory for difference approximations of nonlinear conservation laws and related time-dependent problems, *Acta Numer.*, 12 (2003), 451-512.
- [51] H.Z. Tang and T. Tang, Adaptive mesh methods for one- and two-dimensional hyperbolic conservation laws, *SIAM J. Numer. Anal.*, 41 (2003), 487-515.
- [52] H.Z. Tang, T. Tang, and P.W. Zhang, An adaptive mesh redistribution method for nonlinear Hamilton-Jacobi equations in two- and three-dimensions, *J. Comput. Phys.*, 188 (2003), 543-572.
- [53] T. Tang, Moving mesh methods for computational fluid dynamics, *Contemp. Math.*, 383 (2005), 141-173.
- [54] P.A. Thompson, A fundamental derivative in gasdynamics, *Phys. Fluids*, 14 (1971), 1843-1849.
- [55] M.R. Visbal and D.V. Gaitonde, On the use of higher-order finite-difference schemes on curvilinear and deforming meshes, *J. Comput. Phys.*, 181 (2002), 155-185.
- [56] B. Wagner and W. Schmidt, Theoretical investigations of real gas effects in cryogenic wind tunnels, *AIAA J.*, 16 (1978), 580-586.
- [57] D.S. Wang and X.P. Wang, A three-dimensional adaptive method based on the iterative grid redistribution, *J. Comput. Phys.*, 199 (2004), 423-436.
- [58] Z. Wang, J. Zhu, L. Tian, Y. Yang, and N. Zhao, An efficient fifth-order finite difference multi-resolution WENO scheme for inviscid and viscous flow problems, *Comput. & Fluids*, 230 (2021), 105138.
- [59] A.M. Winslow, Numerical solution of the quasilinear Poisson equation in a nonuniform triangle mesh, *J. Comput. Phys.*, 1 (1967), 149-172.
- [60] K.L. Wu and C.-W. Shu, Entropy symmetrization and high-order accurate entropy stable numerical schemes for relativistic MHD equations, *SIAM J. Sci. Comput.*, 42 (2020), A2230-A2261.
- [61] Y.B. Zel'dovich, On the possibility of rarefaction shock waves, *Zh. Eksp. Teor. Fiz.*, 4 (1946), 363-364.
- [62] H. Zhang, M. Reggio, J.Y. Trépanier, and R. Camarero, Discrete form of the GCL for moving meshes and its implementation in CFD schemes, *Comput. & Fluids*, 22 (1993), 9-23.

- [63] Z.H. Zhang, J.M. Duan, and H.Z. Tang, High-order accurate well-balanced energy stable adaptive moving mesh finite difference schemes for the shallow water equations with non-flat bottom topography, *J. Comput. Phys.*, 492(2023), 112451.
- [64] Z.H. Zhang, H.Z. Tang, and J.M. Duan, High-order accurate well-balanced energy stable finite difference schemes for multi-layer shallow water equations on fixed and adaptive moving meshes, *arXiv: 2311.08124*, 2024.